Kesterite Films Processed with Organic Solvents: Unveiling the Impact of Carbon-Rich Fine Grain Layer Formation on Solar Cell Performance

Ahmed Javed, Doguscan Donmez, Michael D.K Jones, Yongtao Qu, Gorkem Gunbas, Selcuk Yerci**

Ahmed Javed, Gorkem Gunbas, Selcuk Yerci
ODTU-GUNAM, Middle East Technical University, Ankara, 06800, Turkiye
Department of Micro and Nanotechnology, Middle East Technical University, Ankara, 06800, Turkiye
Doguscan Donmez, Gorkem Gunbas
Department of Chemistry, Middle East Technical University, Ankara, 06800, Turkiye
Michael D.K Jones, Yongtao Qu
Department of Mathematics, Physics, Electrical Engineering, Northumbria University, Newcastle Upon Tyne, NE1 8ST, United Kingdom
Selcuk Yerci
Department of Electrical-Electronics Engineering, Middle East Technical University, Ankara, 06800, Turkiye
E-mail: syerci@metu.edu.tr, y.qu@northumbria.ac.uk

Keywords: (kesterites, organic solvents, carbon-rich, fine-grains, nanocrystals)

(Abstract: Solution-processed kesterite (CZTS) solar cells have attracted significant attention owing to their low cost, ease of large-scale production, and earth-abundant elemental composition, which make these devices promising to fulfill the ever-increasing demand of the photovoltaic (PV) industry. Comparable to the performances of expensive vacuum-based techniques, colloidal nanocrystal kesterite solar cells have garnered substantial interest due to their economical and rapid processing. Led by the hot injection method, organic solvent-based techniques have been widely adopted to realize CZTS nanocrystal inks. With organic solvents, ligand-stabilized nanoparticles are formed leading to dispersive and homogenous kesterite inks. However, the presence of carbon-rich ligands around the nanocrystal surface often leads to the formation of a fine-grain (FG) layer that is rich in carbon content. The organic ligands decompose into amorphous carbon residues during a high-temperature annealing process and hinder the grain growth process. The impact of the carbon-rich fine-

grain (CRFG) layer is frequently posed as a negative influence on the PV performance of the kesterite solar cell, however, few reports maintain their disposition about CRFG as innocuous. In this review, a detailed discussion on CRFG is presented, aiming to understand the insights about its formation and impact on the device's performance.)

1. Introduction

According to the World Energy Outlook 2023 report, renewable energy sources (mainly solar and wind) are set to contribute more than 30% of worldwide electricity generation by 2030.[1] Moreover, as compared to 2022, the capacity of renewable energy is expected to increase 3-fold in 2030 where approximately 95% of the growth will be in the form of solar photovoltaic (PV) energy.[1] PV technology holds great potential to dominate industrial, domestic, and commercial markets thanks to its integration potential with, for example, agriculture, buildings, vehicles, IoT devices, etc.[2,3] The promising future of PV technology also poses a supply chain challenge for the industry to meet the ever-growing demands in the coming years. Currently, the global PV industry is majorly based on silicon (Si) technology which covers 96% of solar cells/panels produced worldwide.[4–6] However, with the advent of new technology for PV devices, many versatile materials have been discovered that can offer lightweight and flexible solutions especially suited for system-integrated PV, wearable electronics, and indoor applications.[7,8]

There have been exciting developments among alternative PV materials, including gallium arsenide (GaAs),[9] cadmium telluride (CdTe),[10] copper indium gallium sulfide (CIGS),[11] copper zinc tin sulfide (CZTS),[12] and organic-inorganic halide perovskites.[13] The applications of CdTe, chalcopyrite, and kesterite films in the electronics industry include (but are not limited to) renewable energy devices,[11] thermoelectric devices,[14] optoelectronic devices,[15] and rewritable memory.[16] Thin film technology offers a cost-effective and reliable solution to meet the ever-increasing demands of the PV industry. Perovskite, CdTe, and CIGS-based solar cells are prominent thin film PV technologies and have shown quite decent progress over the past decade.[10–12] However, there have been concerns regarding their composition as they involve scarce, expensive, and toxic elements in their composition.[17–19] Among these, perovskite solar cells possess the highest efficiencies, however, the main issue is their quicker degradation under environmental stressors which not only decreases the shelf life of the device but also hinders electronic activities.[20] Therefore, a growing interest in environmentally friendly CZTS technology has been developed in recent years.

CZTS is a promising material and holds great potential to contribute towards fulfilling the increasing PV demands due to its low-cost, Earth-abundant composition, less toxicity, and facile processing techniques.[21] It offers a direct bandgap and a very high absorption coefficient (~10^4 cm^{-1}), meaning it can be used as a thin-film light-absorbing layer, which reduces material consumption during solar cell production. It is formed by the cationic substitution of group III elements (In and Ga) in CIGS with group II (Zn) and group IV (Sn) making it a I_2-II-IV-VI_4 quaternary semiconductor compound.[22] Adding selenium (Se) into the CZTS stoichiometry has become a common approach, especially after Mitzi's group achieved an impressive kesterite solar cell efficiency of 12.7% with a $Cu_2ZnSn(S_x,Se_{4-x})$ absorber layer.[23] The bandgap can be varied between 0.96 eV to 1.5 eV by tuning the S/Se ratio where higher Se would lead the bandgap closer to 0.96 eV.[24] After the discovery of CZTS as a PV material in 1988,[25] it has been synthesized as a solar energy harvesting layer by many research groups using both vacuum and non-vacuum-based techniques.[26] The stability of the primary kesterite phase exists in a very narrow compositional range,[27] therefore, careful consideration is required while setting parameters in both vacuum and non-vacuum fabrication techniques. Controlling the phase and composition of quaternary CZTS compound during its synthesis can be a challenging task, especially in vacuum-based approaches due to the involvement of multiple elements having different physical and chemical properties, i.e., high volatility of Sn results in Sn loss and can cause phase variations.[28,29] The unwanted variations in the compound's stoichiometric composition may lead to the existence of deep defects, secondary phases, and band gap fluctuations which in turn produce undesirable electronic behavior and eventually high open circuit voltage (V_{oc}) deficits.[30–32] Recently, many strategies have been proposed to elevate the performance of kesterite PV devices by circumventing the issues causing reductions in solar cell output. These strategies include the use of dopants, modified heat treatments, employment of novel passivation layers, and advanced back contact engineering techniques.[33–38] Wu et al. combined the two-step annealing and a controlled Al^{3+} doping to enhance the carrier concentration, reduce defect states, and improve band alignment between CdS and CZTS.[39] An in-situ potassium doping of CZTS precursor led to the suppression of voids and pinholes in CZTS bulk which resulted in a significant efficiency enhancement (10.32-12.62%).[40] Li et al. adopted a machine learning-inspired Gaussian regression algorithm to find out the optimal Mn^{2+} dopant ions ratio in C(Mn)ZTSSe to reduce the Cu/Zn antisite defects which went on to efficiently enhance the V_{oc} and efficiency of the optimized solar cell.[41] Xiao et al. found that replacing the sputtered ZnO window layer with Li-ion doped solution-processed ZnO plays a

passivation role by suppressing interfacial recombination and Fermi-level management.[42] An impressive efficiency of 12.89% was achieved by Yu et al. through the optimization of the selenization process, in particular, the grains‘ composition and structure were improved by controlling Sn loss during annealing.[43] In the last two years, some review studies done on the development of kesterite solar cells have highlighted important facets of this technology and its potential to make promising progress.[44–48] The commercialization of this technology is still limited by the lagging performance of CZTS solar cells in comparison to other mature thin film PV devices such as CdTe and CIGS.[49] Shah et al. have focussed their review study on discussing the roadblocks hindering the efficiency and new strategies to encounter the commonly faced problems in kesterite solar cells.[48] In addition to being used as a primary absorber layer, decent PCEs have been noticed in CZTS-based tandem devices.[50,51] Zhao et al. used the concept of stacking CZTS with C(Cd)ZTS bottom layer to make a flexibly viable solar cell structure. The Cd and Zn ratio in C(Cd)ZTS was adjusted to allow columnar growth of the top CZTS layer by reducing leakage channels.[52] Moreover, owing to the bandgap tunning capability and p-type conductive nature of CZTS films, they have also been used as efficient hole transport layers (HTL).[53–55]

Vacuum-based techniques are well-known for providing uniform and homogeneous CZTS thin films with good reproducibility. Particularly, co-sputtering and co-evaporation are more commonly employed for the fabrication of CZTS(Se) absorber layers which have resulted in respectable solar cell efficiencies.[56–58] However, vacuum methods face several problems that create hurdles in the large-scale production of kesterite absorbers. The confined evacuated space of a vacuum chamber is not conducive to large-area deposition, moreover, the loss of materials during deposition results in less material utilization (much of the material gets coated over the inner walls of the vacuum chamber). The requirements of exceedingly high temperatures and extremely low pressures in vacuum-based techniques demand sophisticated equipment with energy-intensive processing, large capital investment, and costly maintenance. On the other hand, solution-based approaches offer low-cost, fast, and facile processing which leads to high throughput and better scalability for large-scale production.[59] Solution-processed kesterite solar cells have achieved improved efficiencies, which has attracted significant interest among researchers to explore this field.[60] Their potential to provide disruptive and highly efficient kesterite-based PV light absorbers was recently highlighted by a report of 13.8% (certified) power conversion efficiency (PCE) and 14.9% (reported) at the laboratory scale.[61,62] Some examples of solution-based approaches for scale-up applications are, sol-gel,[63] solvothermal,[64] spray pyrolysis,[65] electrodeposition,[66] and

molecular/nanocrystal ink printing.[60,67] Molecular inks are easier to synthesize as compared to nanocrystal inks since they don't require complex steps for dissolution, rather all the precursors are dissolved and allowed to react under mild thermal conditions.[51] Nanocrystal inks (although they require a more complex synthesis) are highly concentrated which is more suitable for large-scale deposition.[68] The synthesis of solution-processed nanocrystal semiconductor devices is increasingly prominent in the thin film semiconductor industry.[69–71] It is well known that Cu-related secondary phases correspond to the occupation of detrimental deep defects, therefore a Cu-poor and Zn-rich composition is desirable in kesterite layers.[72,73] While adjusting the composition of the kesterite layer can be tricky in vacuum-based approaches, the final composition of a kesterite nanocrystal ink is relatively easy to manage by tuning the amounts of precursors and/or the reaction conditions.[74]

Hydrazine serves as a decent solvent with good power to solubilize and cleanly decompose metal precursors (Cu, Zn, and Sn cations), chalcogens (S and Se anions), and metal chalcogenides (CZTS and CIGS).[75–77] The IBM research group has reported consistent progress for hydrazine-based CZTS solar cells which culminated in 2014 with the then-highest efficiency of 12.7%.[23,60,78–81] However, hydrazine-based devices are often criticized for their toxicity and inflammability which require labs to follow extremely strict and tedious safety protocols. For this reason, relatively benign solvents have been widely explored to prepare environment-friendly molecular/nanocrystal inks. Many organic solvents that can dissolve and disperse metal chalcogenides are used for kesterite ink preparation. Dimethylformamide (DMF),[82] dimethyl sulfoxide (DMSO),[83–85] oleylamine (OLA),[67,74,86–92] trioctylphoshphine oxide (TOPO),[93,94] oleic acid (OLE),[95] formamide (FA),[96,97], dodecanethiol (DDT),[98–100] ethanedithiol (EDT),[101] ethanol,[102] methoxyethanol (MEA),[103] and ethylenediamine (EDA),[104] are some of the notable examples of organic solvents successfully implemented for CZTS molecular/nanocrystal ink development.

Given the growing interest of researchers and the promising potential of the solution-processed kesterite films, rapid progress in the last few years has been realized, Wang et al., Benny et al., Fu et al., and Indu et al. have merged the latest reports related to solution-processing of kesterite devices and discussed the up-to-date novel strategies.[105–108] CZTS films prepared from nanoscale solution methods are becoming more desirable since modification of the physiochemical properties of the nanoparticles can be adjusted during synthesis depending on the intended application.[109–111] For applications where electronic communication between adjacent nanoparticles is imperative, doping the nanocrystal ink (with chemical additives) and post-deposition heating treatments are generally adopted to help

suppress excess grain boundaries and defect states for better electrical conductivity between nanoparticle surfaces.[39,112,113] During a nanocrystal ink synthesis with an organic solvent, the organic molecules undergo chemisorbed ligand formation around hydrophobic nanocrystal surfaces, thereby bringing stability and dispersibility to the formed nanoparticles.[114] However, unlike hydrazine-processed films, the organic solvent molecules do not decompose cleanly and often result in the formation of organic impurities in synthesized nanocrystal films.[115] Organic ligands used in the synthesis of inorganic nanoparticles are prone to decomposition during high-temperature annealing. The decomposition of organic ligands leads to polymerization and graphitization, which occur randomly and yield excessive amounts of amorphous carbon impurities on nanoparticle surfaces.[116] Depending on the carbon mass percent (C_{mp}) of the decomposed organic solvent molecule, the conductivity between nanoparticle surfaces is compromised by the presence of randomly oriented carbon chains or matrices which can cause serious current losses in electronic devices. The use of carbon-rich organic solvents, such as OLA (C_{mp} ~ 80%), OLE (C_{mp} ~ 76.5%), and TOPO (C_{mp} ~ 75%), for the formation of CZTS nanocrystals has been known to result in the formation of a CRFG layer at the rear side of the absorber film (in junction with the back contact). Before the annealing step, the entire precursor film (developed from an ink process) is composed of small-sized grains incorporating abundant grain boundaries.[90] The grain growth takes place during high-temperature treatment mainly for passivating grain boundaries and suppressing defect states. The deposited kesterite nanofilms processed with organic solvents are generally heated beyond the boiling point of the used solvent such that solvent molecules are evaporated and do not hinder the grain enlargement process suitable for PV devices. However, it has been seen that the decomposed amorphous carbon residues stay intact at the bottom side and cover the nanoparticle surfaces which restricts the grains' growth resulting in a bi-layer structure composed of LG and FG sub-layers.[90,102,117] This CRFG sub-layer is expected to negatively impact the performance of kesterite solar cells by introducing several problems. An increase in the series resistance is most evident since the FGs in the carbon-rich layer can hinder efficient charge transport.[118] Moreover, a significant imbalance between the composition of FG and LG in solution-processed kesterite films can lead to improper band alignment of the CZTS layer with the back contact.[119,120] It has been reported in some studies that the CRFG is found to be rich in Se and possesses an uneven cation content,[120,121] thus posing a threat to the PCE in terms of potentially abundant secondary phases and band fluctuations near the back contact. The CRFG has also been speculated to not actively participate in the charge conversion process during illumination thereby leading to lesser

charge collection at the electrodes.[90] However, the opinion about the impact of the carbon-rich layer on solar cell performance does not necessarily converge at a common point with some reports claiming that such a layer does not introduce appreciable adverse effects on the PV performance.[122–124] In a study to understand the grain growth process in CZTS during annealing, it was claimed that carbon from organic solvents can assist in rapid growth which in turn is favorable for good PV activity.[124] Furthermore, in the literature, there is a mixture of speculations about the parameters that might influence CRFG formation. While the solvent's C_{mp} directly correlates with the CRFG formation,[125] the inability of the nanocrystal film to get rid of carbon-rich ligands from the nanoparticle surfaces and eventually form CRFG requires clarification.

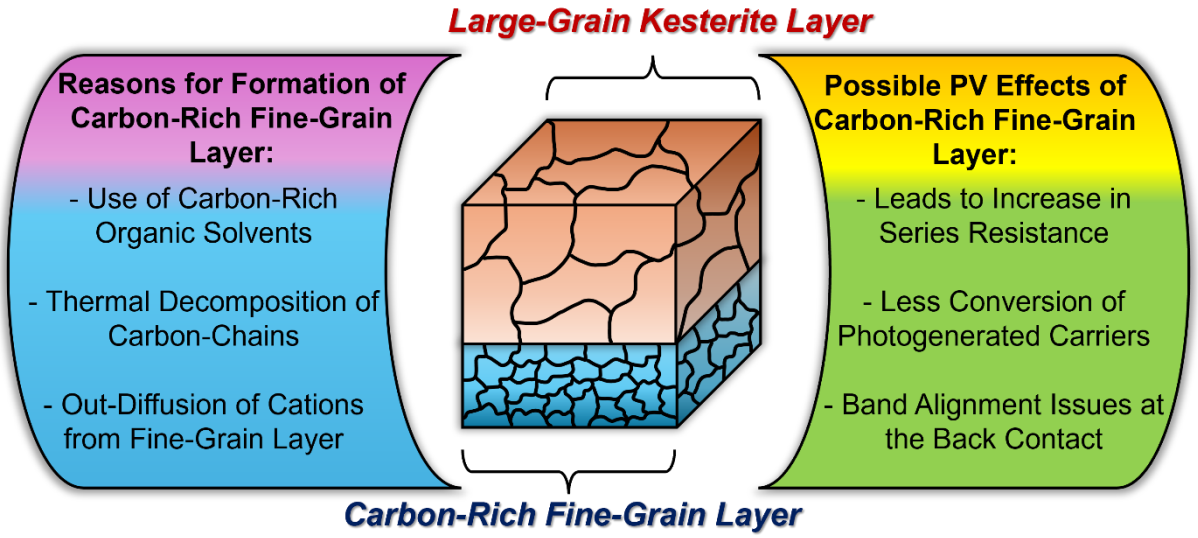

Figure 1. Schematic of a typical kesterite layer processed with an organic solvent containing CRFG sub-layer beneath LG layer along with important points regarding the existence and possible PV effects of CRFG on kesterite solar cell performance.

As the authors of this review, we state that even though the addressed topic holds considerable importance, it has been overshadowed by other issues in kesterite devices and hence not consistently pursued by the research community, therefore, with this dedicated effort, we can trigger a discussion on the CRFG layer among researchers which will help the community to find a consensus that has been missing in the literature. In **Figure 1**, we have summarized the most evident reasons behind the formation of CRFG in solution-processed kesterite layers while the possible factors affecting the PV performance of the solar cell are also mentioned. These points are discussed in detail in the following sections.

In the next section, the colloidal nanocrystal synthesis approach for the formation of CZTS ink is explained in which the procedure and history of a widely used hot-injection method for nanocrystal ink development are briefly discussed. This is followed by a detailed review of the existence of the CRFG layer and its impact on the PV performance of CZTS solar cells in the third and fourth sections, respectively. In the subsequent section, a thorough review of the ligand removal process from kesterite inks and films is presented where ligand exchange/stripping methods are discussed. Lastly, the authors' perspective on the addressed issue is provided in which our recent work on the X-ray photoelectron spectroscopy (XPS) analysis of the lifted-off CZTSSe layer has been included. Our findings based on XPS depth profiling uncover important compositional insights into the CRFG layer while the solar cell capacitance simulator (SCAPS)[126] simulated results on CRFG can lead a pathway toward productive future studies on this topic.

2. CZTS(Se) Colloidal Nanocrystals Synthesis

The synthesis of nanocrystals through colloidal solutions has garnered a vast interest among researchers dealing in electronics applications.[127] The nanocrystal inks formed from colloidal solutions offer several advantages such as compatibility with a variety of coating methods,[128] ability to be coated over flexible substrates,[129] control over nanocrystal's size and shape,[130,131] facile management of nanocrystal composition,[132] and ink's solubility in various solvents for quality enhancement. In semiconductor applications, the use of colloidal nanocrystals is prominent in the synthesis of PV devices, especially metal chalcogenide-based thin film solar cells wherein a colloidal solution containing dispersive and stable semiconductor nanoparticles (nanocrystal ink) is formed and printed/deposited onto a substrate.[133] The colloidal nanocrystal ink method has been employed for the synthesis of absorber layers in various PV devices including, PbSe,[134] CIS,[135] CZTS,[136] CIGS(Se),[137,138] and CdTe.[139] Briefly, nanocrystal ink-based thin films are synthesized by reacting precursors in a high boiling point solvent, subsequently, the ink is deposited onto a substrate followed by an annealing step for the grain's growth. CZTS thin films developed with an ink-based technique can be deposited on a variety of flexible substrates, including plastics,[140] foils,[63] and ultra-thin glass.[141] The coating technique is an important factor in ensuring a uniform and smooth deposition of the precursor ink. Although molecular ink synthesis offers a simpler and facile procedure,[142] nanocrystal inks provide a wider range of freedom over the choice of coating techniques thereby leading to an optimized deposition. A variety of coating methods have been employed for CZTS nanocrystal ink deposition,

including spin coating,[143,144] slot die coating,[89] screen printing,[145] drop casting,[92] and doctor blading.[146] The ability of CZTS nanocrystals to achieve high ink mass concentrations of over 250 mg/ml makes them compatible with cost-effective and scalable industrial coating techniques, such as doctor blading and slot-die coating.[91]

Compared with the facile molecular inks preparation process, a colloidal nanocrystal ink method is a complex route to formulate CZTS inks, nonetheless, nanoparticle-based ink approaches have recently become prominent as they allow a higher degree of freedom over deciding the properties of the developed thin films in terms of a better control over the composition and phase of the formed CZTS nanoparticles which play a crucial role for a better performance in PV applications.[132] Molecular ink-based kesterite solar cells have also resulted in decent PV performances, different works exhibiting solution-processed kesterite solar cells prepared from nanocrystal and molecular inks are shown in **Table 1**. It can be noted in **Table 1** that nanocrystal inks are successfully deposited with a diverse range of coating methods.

A decent nanocrystal ink is characterized by the merits of its stability, uniformity, homogeneity, dispersibility, and concentration. For this purpose, the importance of solvent used for the formation of nanocrystal ink becomes crucial, in that the solvent molecules must provide a conducive environment for the semiconductor nanoparticles to grow and meanwhile keep them from forming agglomerates thus providing the required dispersibility and stability. Both organic and inorganic solvents have been utilized for forming colloidal solutions (or slurries) for CZTS inks. The choice of solvent depends on the nature of the precursors and the conditions under which the reaction takes place. A solvent with a high boiling point is generally considered suitable since the nanoparticle nucleation process takes place at elevated temperatures. Different sources of Cu, Zn, Sn, and S have been used in literature to synthesize kesterite inks, however, generally, metal acetates and metal chloride are preferred since they dissolve well in organic solvents.[108,147] Hydrazine has been a favorite inorganic solvent choice of research groups focused on achieving highly efficient solution-processed kesterite solar cells.[23,60,79,148] However, more recently, given the growing concerns of labs to avoid harmful chemicals in the procedures, the use of hydrazine has become undesirable owing to its extremely flammable nature. This has led to an increased interest in the usage of organic solvents, especially for the synthesis of CZTS nanocrystal inks.

2.1. Organic Solvents for Kesterite Ink Synthesis

Generally, amine-thiol solvents have been used to dissolve metallic precursors and chalcogens for the preparation of several metal chalcogenide nanocrystals. Hexylamine and propanethiol have been used as solvents to prepare a stable mixture of metal precursors and sulfur forming a CZTS molecular ink.[149] It was shown by Lowe et al. that cysteamine diluted with ethanolamine provides a good dissolution of Cu, Zn, Sn, and S particles to form CZTS nanocrystal ink.[150] However, thiols are known to have an unpleasant smell (even in ppm concentrations) in addition to their toxic nature.[151] To achieve efficient kesterite solar cells, DMSO has been employed by several research groups for the formulation of CZTS ink.[84,85,152,153] DMF has also been featured as a solvent in several works that have resulted in decent efficiencies for solution-processed kesterite devices.[154–156] Solvent engineering has been an area of interest wherein calculated proportions of solvents are mixed to enhance the ink concentration, dissolution of particles, and wettability between substrate and ink precursors which altogether can improve the deposition of ink.[99,157–159] Ge et al. showed that the CZTS ink prepared with a mixture of DMF and DMSO provided better wettability between substrate and ink precursors which led to effective deposition and cohesion between ink and substrate.[159]

Table 1. Solution-processed kesterite layers prepared with different organic solvents to form molecular and nanocrystal inks and their efficiencies.

Ref.	Year	Absorber Layer	Solvent	Ink Type	Coating Technique	η (%)
[160]	2020	CZCdTS	MEA	Molecular	Spin Coating	12.6
[152]	2021	CZTSSe	DMSO	Molecular	Spin Coating	12.4
[161]	2016	CZTGeSSe	DMF	Molecular	Spray Coating	11.0
[149]	2015	CZTSSe	Hexylamine + Propanethiol	Molecular	Spin Coating	7.86
[150]	2020	CZTSSe	Cysteamine + Ethanolamine	Molecular	Spin Coating	8.1
[162]	2018	AgCZCdTS	2-Monoethylamine	Molecular	Spin Coating	10.1
[146]	2015	CZTS	OLA	Nanocrystal	Doctor Blading	9.0
[143]	2012	CZTSSe	OLA + TOPO	Nanocrystal	Spin Coating	8.5
[90]	2012	CZTGeSSe	OLA	Nanocrystal	Doctor Blading	8.4
[91]	2010	CZTSSe	OLA	Nanocrystal	Doctor Blading	7.2
[89]	2022	CZTGeSSe	OLA	Nanocrystal	Slot Die Coating	-
[70]	2015	CZTS	EDA	Nanocrystal	-	-

[163]	2014	CZTS	DEG	Nanocrystal	Doctor Blading	2.2
[96]	2015	CZTS	FA	Nanocrystal	Spin Coating	-
[164]	2014	CZTS	OLE	Nanocrystal	Drop Casting	1.66
[165]	2015	CZTS	EG	Nanocrystal	Spin Coating	2.44
[166]	2013	CZTS	TPP	Nanocrystal	Spin Coating	3.6

In the case of nanocrystal synthesis for kesterite inks, OLA has been a prominent organic solvent due to its high boiling point, reducing ability, and control over size, shape, and solubility.[59,167] Apart from their primary role in dissolving the reactants, OLA acts as a capping agent and covers the nanocrystal surface to arrest the grains' growth under specific conditions. Being a coordinating ligand, OLA features a polar head group that develops interaction with the cationic site on the nanocrystal surface and a long aliphatic alkyl chain to allow stabilization and dispersion via steric repulsion between nanoparticles.[168] OLA and TOPO are often used together to provide enhanced stability to CZTS nanocrystals and achieve optimal reaction conditions.[169,170] TOPO possesses good control over the growth kinetics of nanoparticles.[171,172] Other than these, organic solvents that are comparatively low in carbon have also been used to develop CZTS nanoparticles that include, ethylene glycol (EG), diethylene glycol (DEG), and FA, however, their performances are not as good as OLA-processed CZTS films which explain the ubiquitous use of OLA solvents.[96,165,173,174] Moreover, FA-processed CZTS films have been observed to be porous and abundant in voids.[97,175] In **Table 2**, the chemical structures, densities, and boiling points of various organic solvents having different carbon mass percents commonly employed for the synthesis of CZTS nanocrystals have been shown.

Table 2. Details of organic solvents frequently used in literature to synthesize kesterite inks.

Solvent	C_{mp}	Boiling Point (°C)	Density (g/mL)	Chemical Structure	Some Works in Kesterite Inks Preparation
Oleylamine ($C_{18}H_{37}N$)	81%	348-350	0.813	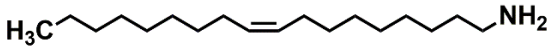	[74,90–92,176]
Oleic Acid ($C_{18}H_{34}O_2$)	76.5%	359-361	0.89	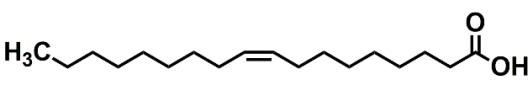	[95,164,177,178]

Trioctylphosphine Oxide ($C_{24}H_{57}OP$)	75%	212-213	0.88	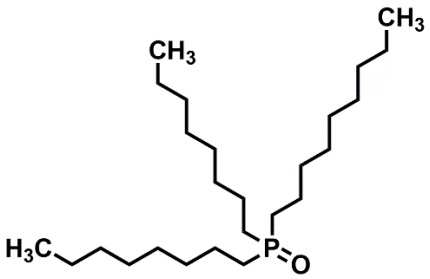	[143,169,170]
Diethylene Glycol ($C_4H_{10}O_3$)	45%	245-246	1.118	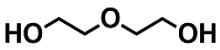	[163,179]
Ethylenediamine ($C_2H_8N_2$)	40%	117-118	0.899	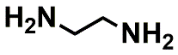	[180,181]
Formamide (CH_3NO)	27%	210	1.134		[96,97]

2.2. Hot Injection Method

In the case of a typical ink synthesis method for chalcogenide-based thin films, the metal precursors are dissolved in a coordinating ligand-forming solvent which not only provides dissolution to the precursors' ions but also acts as a capping agent to the nanoparticles. The nanoparticles are formed as a result of burst nucleation at elevated temperatures. The initial amounts of precursors dissolved in a solvent can be adjusted to get the desired composition. Moreover, the solvent concentration also influences the structure, morphology, and optical properties of the nanocrystals. Xia et al. noticed an increase in the bandgap of CZTS nanocrystals from 1.34 eV to 1.61 eV when the DDT concentration was increased in the precursor solution.[98]

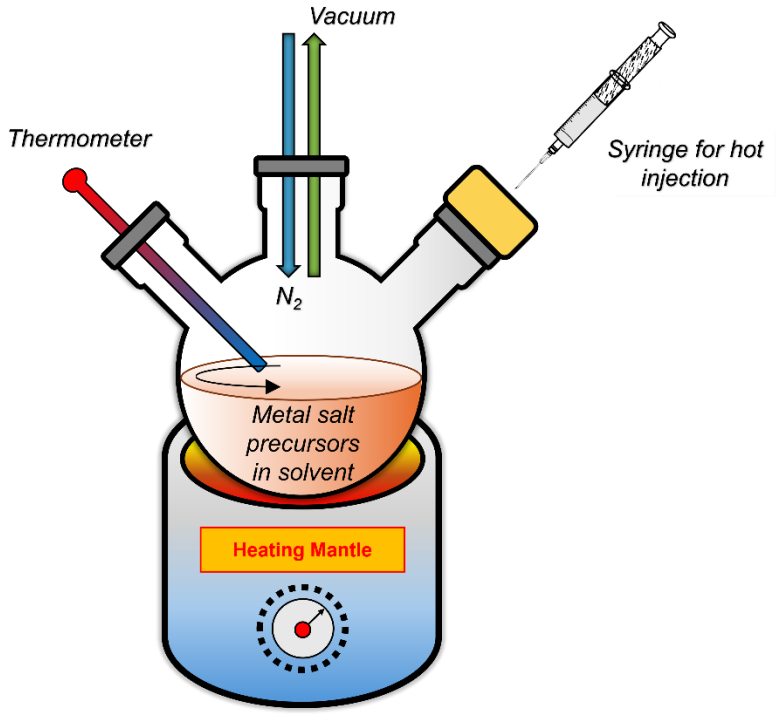

Figure 2. A three-neck flask containing metal salt precursors dissolved in a solvent mounted on a heating mantle depicting a typical hot injection process.

In 2003, Joo et al. proposed the idea of injecting elemental sulfur dissolved in OLA at a high temperature in a solution containing metal salt precursors mixed with a combination of OLA and TOPO solvents.[182] They demonstrated successful synthesis of dispersible and stable PbS, ZnS, CdS, and MnS nanocrystals. This strategy attracted great interest in the synthesis of ternary and quaternary semiconductor nanocrystals owing to their simplicity, cost-effectiveness, and decent compositional control. This process was later called the hot injection method and was used by Guo et al. in 2009 to synthesize CZTSSe nanocrystals and later for CZTS nanocrystals by Steinhagen et al.[92,183] A typical depiction of the hot injection process is shown in **Figure 2,** where metal salt precursors are dissolved in a solvent inside a three-neck flask while the three inlets are used for connection with the Schlenk line, sulfur injection, and temperature monitoring, the setup is mounted on a heating mantle. Guo et al. formed a CZTS nanocrystal layer from nanoparticle ink synthesis where OLA was used as the sole solvent to dissolve Cu, Zn, and Sn salt compounds contained in a three-neck flask. The mixture temperature was first elevated to 130^{o}C and then to 225^{o}C after waiting for 30 mins. At the reaction temperature of 225^{o}C, elemental sulfur mixed in OLA was injected into the flask through one of the inlets which labeled this process as the “hot injection method”. The mixture was kept at the reaction temperature for another 30 mins and then naturally cooled down to allow the nucleation process of CZTS nanocrystals. At the end of the reaction, a

dark-colored ink was formed which was subjected to centrifugation several times before adding toluene and isopropanol to redisperse the solution. Finally, the concentrated ink was coated onto a soda lime glass substrate using drop cast deposition. Successful demonstration of CZTS nanocrystals with sizes ranging between 15-25 nm was depicted through X-ray diffraction spectroscopy (XRD) and their semi-conducting behavior was confirmed by ultraviolet-visible (UV-vis) absorbance spectroscopy measurement showing a bandgap of 1.5 eV. The deposited films were subsequently annealed at 500°C for 20 mins in a selenium-rich environment to convert CZTS into CZTSSe nanocrystals. Although this research showed the viability of the hot injection method for CZTS nanocrystal formation, the PCE of the solar cell turned out to be only 0.80%.[92] In 2010, the same research group reported an impressive PCE of 7.2% by adjusting the composition of the developed kesterite layer. The cations concentrations were tuned in such a way as to yield a Cu-poor and Zn-rich composition thereby eliminating the Cu-related binary or ternary phases causing a significant improvement in efficiency. They also used hexanethiol as an additional step to redisperse the dried ink forming a stable and concentrated nanocrystal ink of 200 mg/ml.[91] With a few modifications, this synthesis template has been followed by several research groups for the formation of CZTS nanocrystal inks,[67,146,169,173,184] some of them are explained in **Table 3**.

Table 3. Solution-processed kesterite layers prepared with different organic solvents to form molecular or nanocrystal inks and their efficiencies.

Ref.	Metal Compounds Precursors	Solvent	Reaction Conditions	Injection Content	Nanocrystals Size (nm)	Eg (eV)	Annealing Conditions	PCE (%)
[92]	1.50mmol $Cu(acac)_2$, 0.75mmol $Zn(acac)_2$, 0.75mmol $Sn(acac)_2$	OLA	225°C for 30 mins	3mmol Sulfur + 3ml OLA	15-25	1.5[a)]	Selenized at 500°C for 20 mins	0.80
[91]	1.332mmol $Cu(acac)_2$, 0.915mmol $Zn(acac)_2$, 0.75mmol $Sn(acac)_2$	OLA	225°C for 30 mins	4mmol Sulfur + 4ml OLA	-	1.05	Selenized at 500°C for 20 mins	7.2
[185]	1mmol $Cu(acac)_2$, 0.5mmol $Zn(acac)_2$, $Sn(acac)_2Cl_2$[b)]	OLA	280°C for 60 mins	a: 5ml of 0.1M $GeCl_2$ in OLA b: 2ml of 1M Sulfur in OLA	13.3	1.40	Selenized at 500°C for 20 mins	6.8
[90]	1.275mmol $Cu(acac)_2$, 0.9mmol $Zn(acac)_2$, 0.525mmol $Sn(acac)_2Br_2$, 0.225mmol GeCl	OLA	225°C for 30 mins	4.5mmol Sulfur + 4.5 ml OLA	5-15	1.09	Selenized at 500°C for 20 mins	8.4
[169]	0.5mmol $Cu(acac)_2$, 0.25mmol $Zn(OAc)_2$, 0.25mmol $Sn(OAc)_4$	OLA + TOPO	300°C for 75 mins	1mmol Sulfur + 1ml OLA	12.8 (±1.8)	1.5	-	-
[146]	1.32mmol $Cu(acac)_2$, 0.79mmol $Zn(acac)_2.H_2O$, 0.75mmol $Sn(acac)_2Cl_2$	OLA	250°C for 60 mins	4.5mmol Sulfur + 4.5ml OLA	12.51 (±7.94)	1.1	Selenized at: a: 500°C for 40 mins b: 550°C for 20 mins	9.0

[173]	0.4mmol $CuCl_2.H_2O$, 0.45mmol $Zn(OAc)_2$, 0.2mmol $SnCl_4.5H_2O$	DEG + TETA[c)]	220°C for 120 mins	1mmol Sulfur + 0.5ml TETA + 1ml DEG	23 (±11)	1.44	-	-
[186]	0.3506mmol $Cu(acac)_2$, 0.2156mmol $Zn(OAc)_2$, 0.1875mmol $Sn(OAc)_4$	OLA + TOPO	325°C for 45 mins	1.32mmol (S and Se) + 0.8 mmol $NaBH_4$ + 3ml OLA	7.8-11	1.47-1.54	-	-
[99]	2mmol $CuCl_2$, 1.5mmol $ZnCl_2$, 1.09mmol $SnCl_2$	OLA + DDT	270°C for 30 mins	5.6mmol Sulfur + 5ml DDT + 3ml OLA	300-500	1.5	Sulfurized at: 500-600°C for 2hrs	-

[a)](Before selenization); [b)]Depended on Ge/Sn ratio; [c)](Triethylenetetramine)

Some of the efforts highlighted a few improvements to further improve the uniformity and size distribution of nanocrystals by modifying different parameters. Riha et al. slightly varied the technique and used TOPO in combination with OLA as solvents and capping ligands to carry out the synthesis of CTZS nanocrystals which showed better mono-dispersibility.[169] Qu et al. studied the influence of reaction conditions on the composition and structure of CZTS nanocrystals. The dependence of crystal properties on varying reaction temperatures and durations was explored. It was found that the crystal size increased from 4.4 nm to 11 nm when the reaction temperature was increased from 195°C to 240°C. Moreover, an increase in the bandgap from 1.42 eV to 1.84 eV was noticed when the reaction duration was changed from 15 to 60 mins. Another important finding was that Cu-poor and Zn-rich composition was achieved at and after 30 mins of reaction time. The reason for Cu-rich composition at shorter durations of reaction was explained by a higher affinity of Cu cations to associate with S anions initially, and after the reaction was given enough time Zn and Sn diffused into the nanocrystal to form the CZTS phase.[74]

3. Formation/Existence of CRFG in Kesterite Films

Although the CZTS nanocrystals produced with an organic solvent provide a relatively less toxic alternative to hydrazine-processed absorber films, it comes with the disadvantage of forming a carbon-rich insulating capping ligand around the nanocrystal surface.[102,187] The organic coordinating ligands are generally composed of long hydrocarbon chains having a carbon-rich composition which are responsible for introducing organic impurities in the kesterite nanocrystal layer. Generally, the FG layer is absent in hydrazine-processed and vacuum-based CZTS(Se) films which only feature an LG monolayer structure as can be seen in **Figure 3**. However, the existence of an FG layer is frequently reported in CZTS(Se) nanocrystal films prepared with carbon-rich organic solvents such as OLA, OLE, TOPO, etc. Many publications have reported the presence of a CRFG layer at the rear side of a solution-

processed absorber layer and an increased interest in understanding its implication on solar cell performance has been noticed in recent years.[90,102,117,120,125,143,164,175,187] The presence of the CRFG layer between the CZTS(Se) layer and substrate becomes evident in the SEM images taken after the annealing step as shown in **Figure 4**.

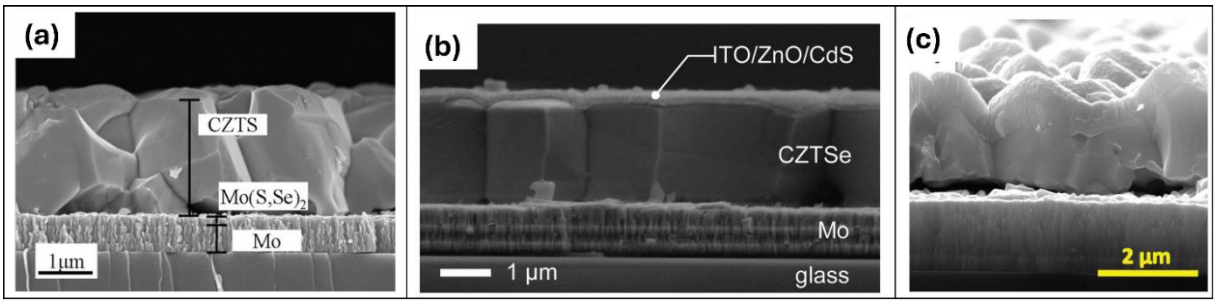

Figure 3. Cross-sectional SEM images of CZTS(Se) films showing monolayer structure prepared with; (a) hydrazine solutions, reproduced with permission.[60] 2014, Wiley, (b) co-evaporation process, reproduced with permission.[188] 2015, Wiley, and (c) co-sputtering process. Reproduced with permission.[189] 2018, Wiley.

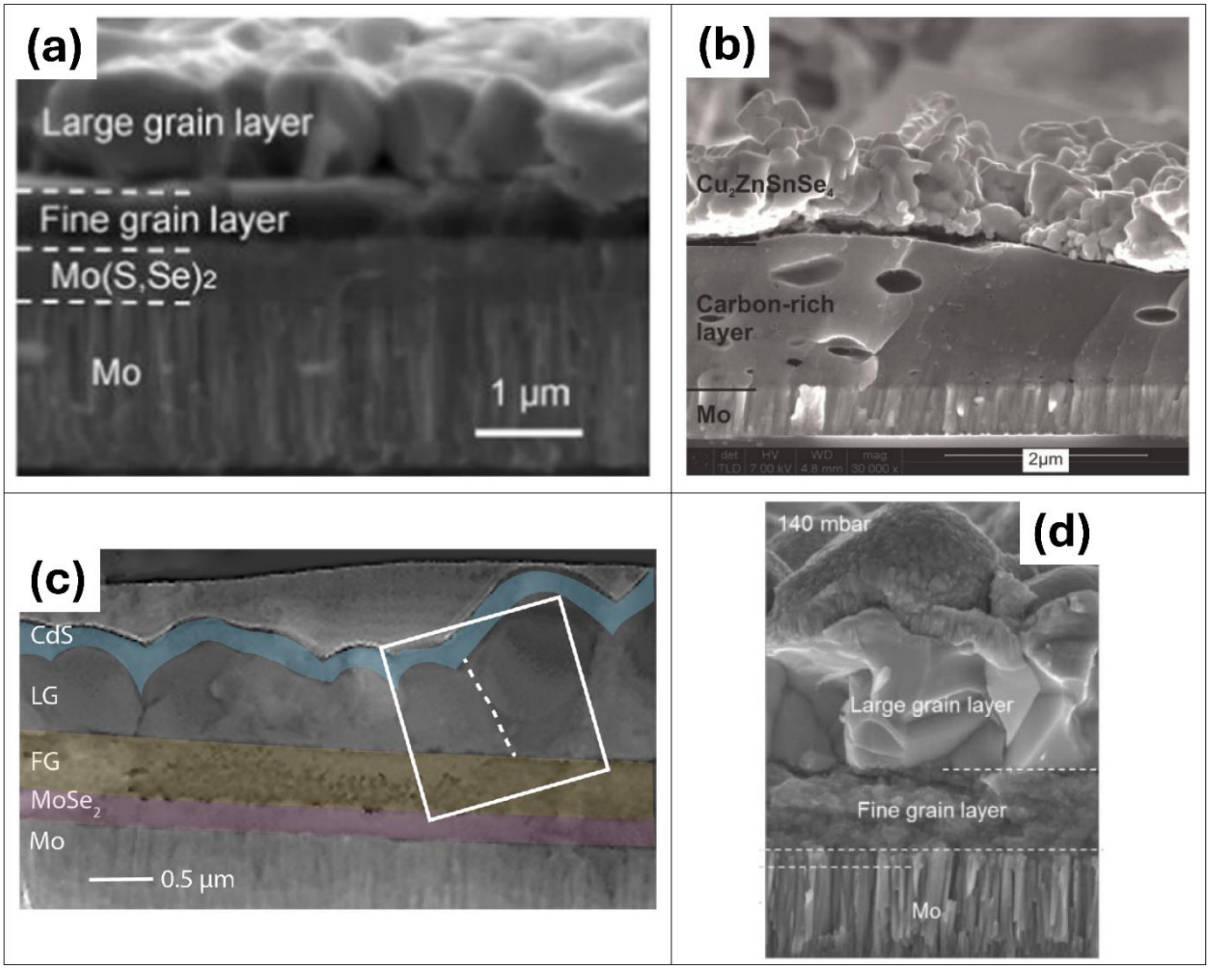

Figure 4. (a) SEM cross-section for FG and LG in CZTS solar cell structure. Reproduced with permission.[87] 2016, Wiley. (b) Cross-sectional SEM image of the CZTS layer with an evident FG layer. Reproduced with permission.[190] 2012, Wiley. (c) Cross-section HAADF-STEM image of CZTS solar cell with distinguishable LG and FG. Reproduced with permission.[191] 2021, American Chemical Society. (d) SEM cross-section of a CZTSSe solar cell structure with a distinctive CRFG structure. Reproduced with permission.[88] 2018, IOP publishing.

Upon the deposition of a CZTS precursor ink on a substrate, the entire nanocrystal film is thought to be composed of very small grains with abundant interface boundaries before a high-temperature annealing step is performed.[121,124,175] During the selenization step, the small CZTS grains evolve into larger CZTSSe grains which are favorable for carrying out the PV activity.[120] The process of selenization has become a routine in kesterite solar cell synthesis which not only adds Se into the chemical stoichiometry of the CZTS nanoparticle film but also initiates a recrystallization process to enhance the film's quality during high-temperature treatment.[192] Selenization usually takes place in a vacuumed quartz tube furnace. The nanoparticle film is placed with a carefully calculated amount of Se pellets in a graphite box while the annealing temperature is set to somewhere around 450-550^{o}C and a standard annealing time ranges from 20-40 mins.[87] However, several modified approaches have been proposed in literature to achieve better crystallinity which also includes the use of H_2Se gas as a Se source.[193] For CZTS nanocrystal films without Se, annealing is performed with sulfur vapors or with sulfide powders to allow crystal growth.[164] It is well known that the high-temperature annealing step allows the grain enlargement process crucial for PV performance, however, the persistence of FGs at the rear side of the CZTSSe absorber post-annealing treatment can be ascribed to the thermal decomposition of organic solvent molecules which restricts the growth of the grains. It has been suggested by Yanyan et al. that the FG layer contains a high amount of carbon in the form of an amorphous matrix which is embedded with binary and ternary chalcogenide phases.[143] The presence of high amounts of carbon in the FG layer of a CZTS(Se) layer is confirmed through elemental profiling in many works, a few of which are shown in **Figure 5**.

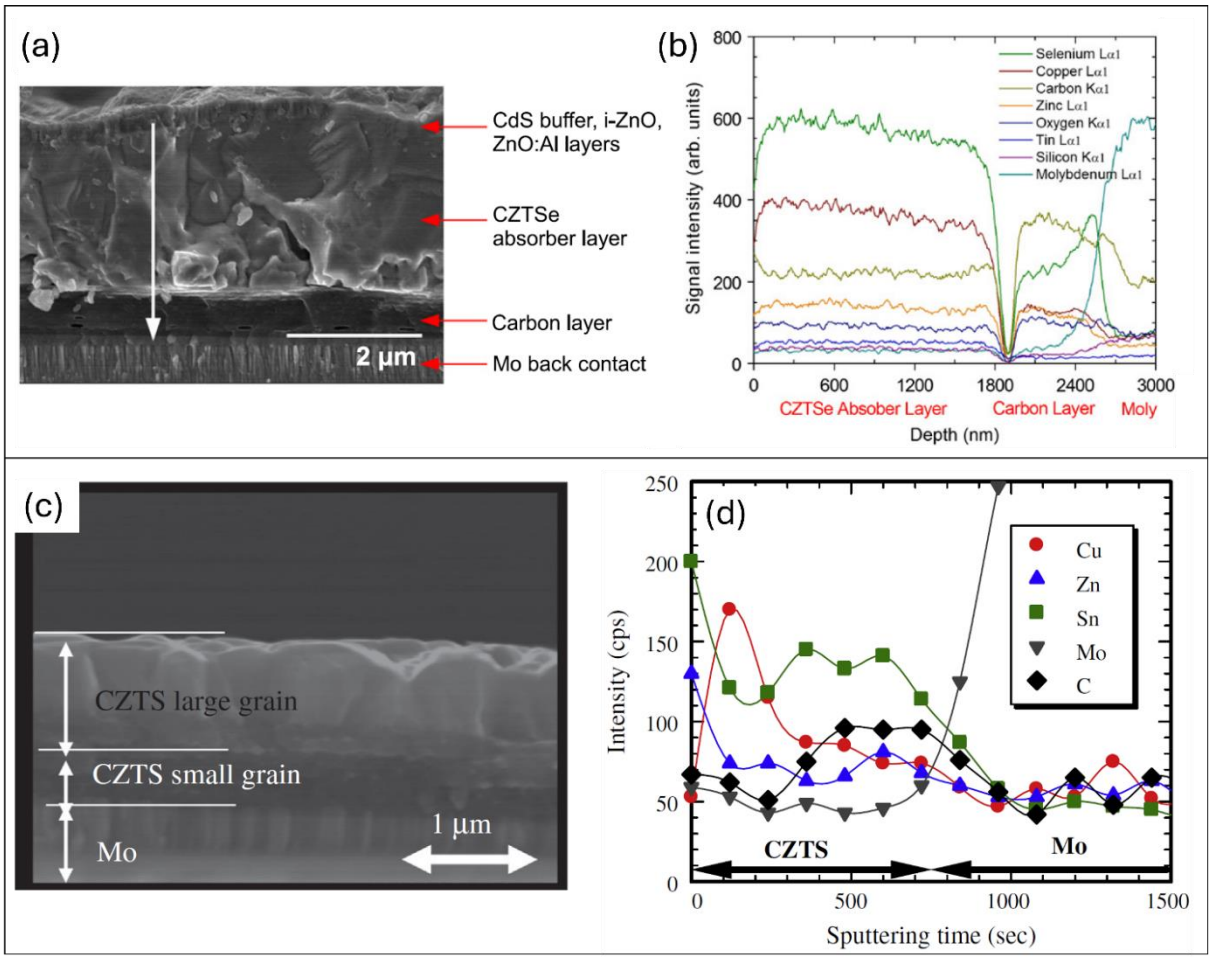

Figure 5. (a) SEM image of CZTSe solar cell showing a distinctive CRFG layer and (b) EDS depth profile of SEM image shown in (a) representing a carbon-rich composition at the FG layer. Reproduced with permission.[187] 2012, Elsevier. (c) Cross-sectional SEM image of the CZTS layer with small and LG layers and (d) the EDS depth profile of the corresponding SEM image showing carbon being high in the small grain layer. Reproduced with permission.[117] 2014, Elsevier.

The organic ligands occupying the top side of CZTS film are mostly evaporated during annealing thus providing a conducive environment for grain growth while the failure of bottom side nanocrystals to get rid of bulky organic ligands becomes a primary reason for the existence of CRFG layer in junction with the back contact. Chernomordik et al. studied the grain growth of OLA-CZTS nanocrystals during annealing treatment in a sulfur-rich environment. Their study found that the carbon content decreased from 20-25% to 10-15% as the grain sizes increased during the annealing treatment. The carbon evaporated in the form of volatile CS_2 and COS compounds after reacting with sulfur. However, they did not observe a bi-layer structure with a distinctive carbon-rich layer, rather carbon was distributed uniformly

through the layer.[164] Later, the same group noticed a distinctive FG layer when CZTS film was selenized at 700ºC for 1 hr.[194] Based on this, it was claimed in their work that as compared to selenization, sulfurization provides a better environment for the evaporation of carbon atoms from the vicinity of nanocrystals. Although both sulfur and selenium atoms can penetrate deep into the CZTS layer and form volatile compounds (CSe_2 and CS_2), the CSe_2 molecules have more chances to get trapped into the crystals and polymerize thereby leading to high carbon content in the FG layer.[195] On the other hand, the small grain layer in CZTS film treated with sulfurization was claimed to be poor in carbon due to efficient removal during the annealing process.[194] Contrary to this, Tong et al. found that a distinctive FG was present in CZTS nanocrystal film annealed in a sulfur-rich environment. The evaporation of organic residues from the top side nanoparticle surfaces took place as sulfur could thoroughly interact with the solvent molecules, however, the physical barrier faced by sulfur molecules to diffuse to the bottom of the film deprived the back side grains of sulfur interaction and hence the carbon residue stayed intact.[125] It was found by Yan et al. that selenium vapors also failed to penetrate toward the bottom of the CZTS layer during the selenization process which led to the formation of a CRFG layer.[196] As can be noticed in the schematic given in **Figure 6(b),** Tanaka et al. stated that the formation of a CZTS large-grain layer caused the blockage of carbon evaporation during the thermal annealing process, which eventually led to the formation of a carbon-rich layer beneath large-grains.[117] However, this was disputed by Chernomordik et al. who stated that their EDS analysis revealed carbon-rich composition at positions in FG that were not covered with LGs on the top.[194] For a better supply of Se at the bottom side, Hages et al. proposed a liquid-assisted grain growth mechanism wherein Se in liquid form was deposited beneath the CZTS nanocrystal film before the selenization process.[113] This would allow initial nucleation and crystallization at the liquid-solid interface while cations are supplied from the nanoparticle film leading to an LG CZTSe layer at the bottom as shown in **Figure 6(a)**. However, their strategy led to the existence of an FG layer at the top side, hence giving rise to a flipped bi-layer structure. This might have happened due to the lack of cations available at the top side which is considered important for the grain enlargement process.

Mainz et al. studied the evolution of the kesterite phase during the selenization process. They have concluded that the accumulation of a carbon-rich layer beneath the LG CZTSSe layer can be explained by the out-diffusion of cations from the bottom side nanocrystals. This would not only assist the growth of nanoparticles at the top but also increase the carbon density at the bottom. A Cu_xSe phase would provide favorable conditions for CZTSe LG

formation and the deprivation of Cu at the bottom side would eventually lead to the formation of CRFG.[120] Hauschild et al. corroborated this idea and mentioned that the carbon-rich layer is mainly composed of C, S, and Se content.[123]

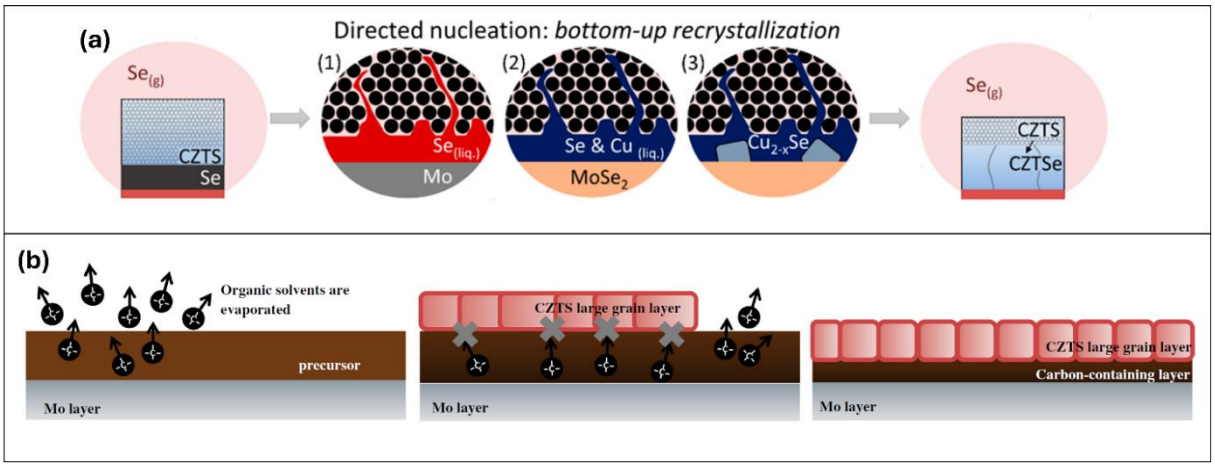

Figure 6. (a) Liquid Se assisted bottom-up grain growth approach. Reproduced with permission.[113] 2016, American Chemical Society. (b) Schematic showing the concept behind the evaporation of carbon atoms from the top side and trapping of bottom ones during annealing. Reproduced with permission.[117] 2014, Elsevier.

The thickness of the FG layer is likely to be dependent on the solvent used for dissolution during synthesis. The amount of carbon residues left behind after annealing can be related to the number of carbon atoms per molecule of the organic solvent used for the synthesis of CZTS film.[125] As can be observed in **Figure 7(d,g,h)**, a CZTS layer synthesized with OLA is expected to form a thicker FG due to the rich carbon content of an OLA molecule (18 carbon atoms per molecule). For the same reason, a CZTS nanocrystal film processed with FA solution should not exhibit a distinctive FG layer given the fact that a single FA molecule has only one carbon atom. This was confirmed by some studies that experimentally confirmed the non-existence of a distinctive FG layer in FA-processed CZTS film (**Figure 7(c)**).[96,97,175] Furthermore, the grains of nanocrystal film covered with shorter hydrocarbon chains grow to a higher degree as compared to those that are covered with carbon-rich ligands.[125] Huang et al. studied the grain growth mechanism of CZTS-OLA nanocrystals during annealing and compared them with CZTS-FA nanocrystals to find out the differences in their microstructural evolution which is crucial in understanding the formation of FG layer in CZTS-OLA films. Contrary to CZTS-FA, the grain enlargement in CZTS-OLA film was noticed to be abnormal in such a way that the nanocrystals existing at the top side of the films

grew at a faster rate than the bottom ones and the reason for such a polarity was attributed to the presence of bulky OLA-based carbon-rich ligands at the rear side. The OLA ligands present at the top side of the film were easily evaporated during annealing while the bottom ones stayed intact and hindered the grain growth process. Finally, they reported that there was no distinctive CRFG layer in CZTS films developed with FA-based solution **(Figure 7(e,f)**. However, there was a higher percentage of voids in CZTS-FA films which made the layer more porous and less effective for generating a PV response as compared to CZTS-OLA film.[175] A depiction of voids in FA-processed CZTS film can be seen in **Figure 7(a)** while **Figure 7(b)** showcases a packed LG CZTS layer accompanied by a carbon-rich layer for OLA-processed film.

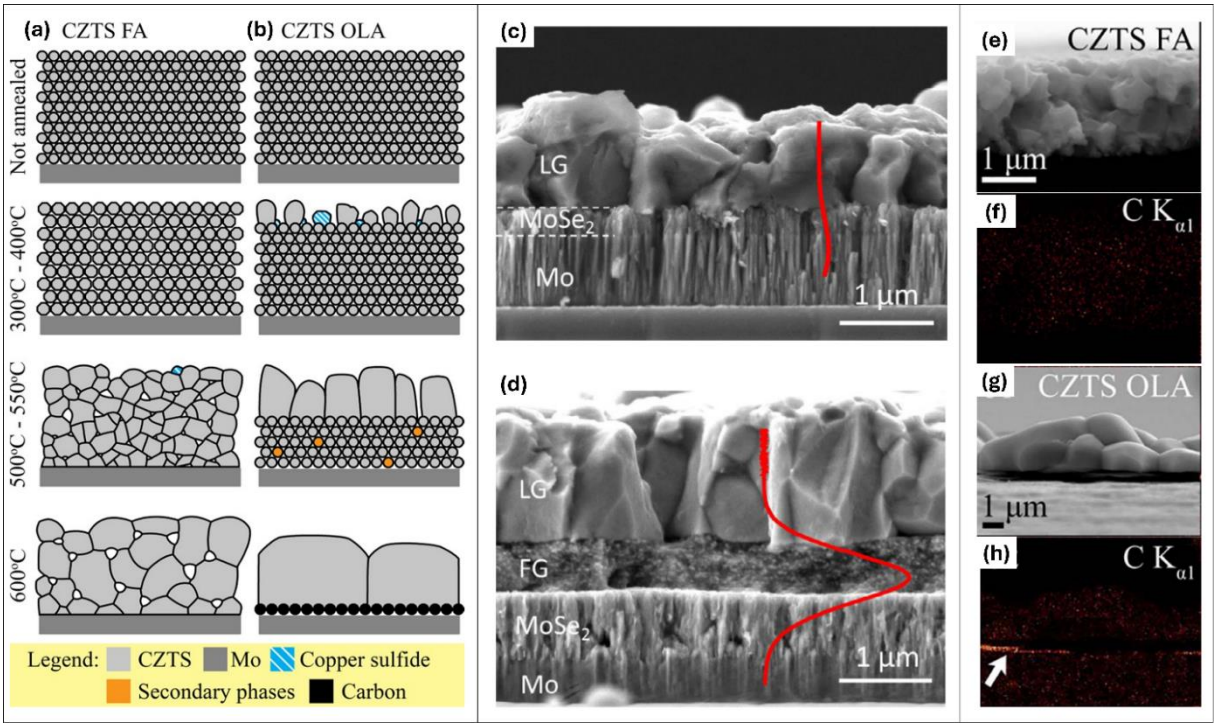

Figure 7. (a,b) Schematic showing microstructure evolution of CZTS-FA and CZTS-OLA during annealing treatment. Reproduced with permission.[175] 2016, Wiley. (c) SEM cross-section of CZTS-FA film without the existence of CRFG (red line showing the carbon profile along the cross-section) and (d) CZTS film prepared with OLA featuring a distinctive FG layer. Reproduced with permission.[174] 2018, Elsevier. (e,f) SEM image of CZTS-FA film along with EDS area scan and (g,h) SEM and EDS scan of CZTS-OLA film showing a carbon-rich layer between CZTS layer and molybdenum (Mo) contact. Reproduced with permission.[175] 2016, Wiley.

4. Impact of CRFG on PV Performance

For both CIGS(Se) and CZTS(Se), near-micron-sized crystals are often desired for better PV performances.[132,197,198] The LG layer of the CZTS absorber is mainly responsible for carrying out the PV activity of the device because of reduced grain boundaries.[121,125] On the other hand, the FG layer being in junction with the back contact can limit the performance of kesterite solar cells by introducing several drawbacks including, an increase in series resistance, recombination paths/centers, bandgap fluctuations, reduced absorption, and formation of secondary phases due to composition variation.[117,120,143,199–201] However, few papers have speculated the benign nature of the carbon-rich layer on solar cell performance and few have even reported the suitability of carbon content in the FG to conduct charge carriers and assist in rapid grain growth.[122–124,202,203] Although there remains a slight uncertainty about the real impact of the CRFG layer on solar cell overall performance, the general notion is skewed toward the negative aspect of the CRFG layer.

Based on a simulated modeling approach on SCAPS to calculate the FG layer thickness effects on the PV response, Wu et al. concluded that the FG layer does not pose a threat to the overall efficiency of the CZTS device and claimed that the experimentally measured PCE is not appreciably affected as well.[122] Moreover, Huaschild et al. speculated the carbon-rich layer can effectively extract holes and referred to it as an HTL.[123] Nevertheless, systematic experimental studies to uncover some important aspects of the CRFG are needed for quantifying its real impact on PV performance. Campbell et al. found that with the absence of a CRFG layer at the rear side of a CZTS absorber film, the PCE of the device increased where the main contributor to the efficiency enhancement was a higher fill factor (FF).[174] Miskin et al. reported improvement in the PCE of the OLA-processed CZTSSe device from 7.2% to 9.0% by decreasing the FG layer thickness achieved by modifying selenization conditions.[146] Wang et al. reported that one of the factors limiting the current density of a solution-processed CZTS solar cell at 23.46 mA/cm^2 was the existence of a 400 nm CRFG between $MoSe_2$ and CZTS LG.[102] Embden et al. found that the PCE increased from 6.53% to 7.68% by simply avoiding the CRFG layer and achieving a monocrystalline absorber film in CZTSSe solar cells.[118] Tanaka et al. also reported an increase in PCE from 0.35% to 0.63% as the CRFG layer became thinner.[117] In addition to these studies, few other researchers have also mentioned the detrimental PV effects caused by CRFG in kesterite devices which upon reduction or removal have shown better performances.[204,205] There remains a question mark of whether the contribution of carbon content in the FG layer has an adverse effect(s) on the solar cell output parameters. Investigations done by Tiong et al. might serve to explain the correlation between the C_{mp} of solvent molecules and the current loss mechanism. They

prepared multiple CZTS films with different organic solvents and found that the film prepared with the solvent having the least C_{mp} generated the best photocurrent value. The current density of CZTS film prepared with glycerol having 3 carbon atoms per molecule was recorded as 0.43 mA/cm^2 which was far better than 0.15 mA/cm^2 produced by 1,7-heptanediol processed film.[125] Furthermore, a commonly used practice to exchange/strip carbon-rich ligands from CZTS nanocrystals has resulted in appreciable PCE improvements.[168,206–208] Khanzada et al. showed that reducing carbon-rich ligands from CZTS nanocrystal film used as an HTL increased the PCE of a perovskite solar cell from 12.2% to 15.4%. Therefore, it is expected that the improvement in the device‘s efficiency is caused by a reduction in carbon content which eventually leads to FG minimization.[205] Based on our review study, the different factors that might influence the output parameters of kesterite solar cells featuring a CRFG layer have been categorized into the following sub-headings.

4.1. Series Resistance

It has been routinely reported that the CRFG in kesterite solar cells contributes towards increased series resistance which can negatively affect PCE by mainly reducing the FF.[90,102,143,187,209] The relatively amorphous nature of the FG layer makes it difficult for the charge carriers coming from the LG layer to reach the back contact. The charge transport blockage in the FG layer increases series resistance which is reflected by reduced J_{sc} of the device. Tanaka et al. found that the J_{sc} and series resistance values were most affected when the CRFG thickness was minimum (J_{sc} increased and series resistance decreased).[117] On the other hand, Hauschild et al. and Cao et al. suggested the presence of amorphous carbon content in the FG layer makes the CZTS device electrically conductive at the back contact.[123,143] This was not the case in the findings of Embden et al. who noticed a significant 94% reduction in the series resistance after converting the bi-layer structure (LG + CRFG) to a single layer composed of only LG in a CZTSSe solar cell.[118] Using electron beam-induced current (EBIC) measurements, Kogler et al. found that even though CRFG provides a conducting passage to charge carriers, only the upper LG layer generates charge carriers for collection.[210]

4.2. Mobility of Charge Carriers

While capping ligands are important in keeping the formed nanoparticles from creating agglomerates and maintaining the dispersibility of ink,[211,212] they might hinder nanoparticles

from participating in semiconducting processes due to their insulating nature.[115,213,214] For semiconductor applications, the nanocrystal surfaces need to be well passivated and electronically coupled with each other to ensure an effective charge extraction and transport. However, the nanocrystals surrounded by bulky organic ligand chains are separated with larger inter-particle distances which hampers the electronic communication between them making the charge transport harder.[213] The most used capping ligands feature long hydrocarbon chains and hence the abundance of carbon is expected in the regions covered with organic ligands.[118,208,215] For CZTS nanocrystal ink synthesis, OLA has been ubiquitously used as a solvent and capping agent for nanoparticle development as can be noticed in **Table 3**. A comparison of an OLA ligand with other organic ligands has been shown in **Figure 8(a)** where the longest length of carbon chain possessed by OLA is quite evident. Kim et al. used triphenylphosphate (TPP) molecules as capping ligands for CZTS nanocrystals to replace the long tails of aliphatic OLA with relatively compact aromatic TPP ligands. Although stable nanocrystals were developed with TPP ligands, the PCE was just about 3.4%.[166] CZTS nanocrystals covered with long OLA-based ligands face lower carrier mobility issues, in that a higher effective mass of the nanocrystals makes the movement of charge carriers difficult within the lattice. It was found by Huang et al. that the carrier mobility of CZTS-OLA nanocrystals was 29 times less than the CZTS nanocrystals prepared with 1-butanethiol (BTT) which feature a shorter ligand length. They also reported a large difference in the ligand percentage of CZTS nanocrystals between OLA (23.32%) and BTT (3.36%) while the higher masses of OLA-CZTS nanocrystals were confirmed by thermogravimetric analysis (TGA) measurements as shown in **Figure 8(c)**.[214]

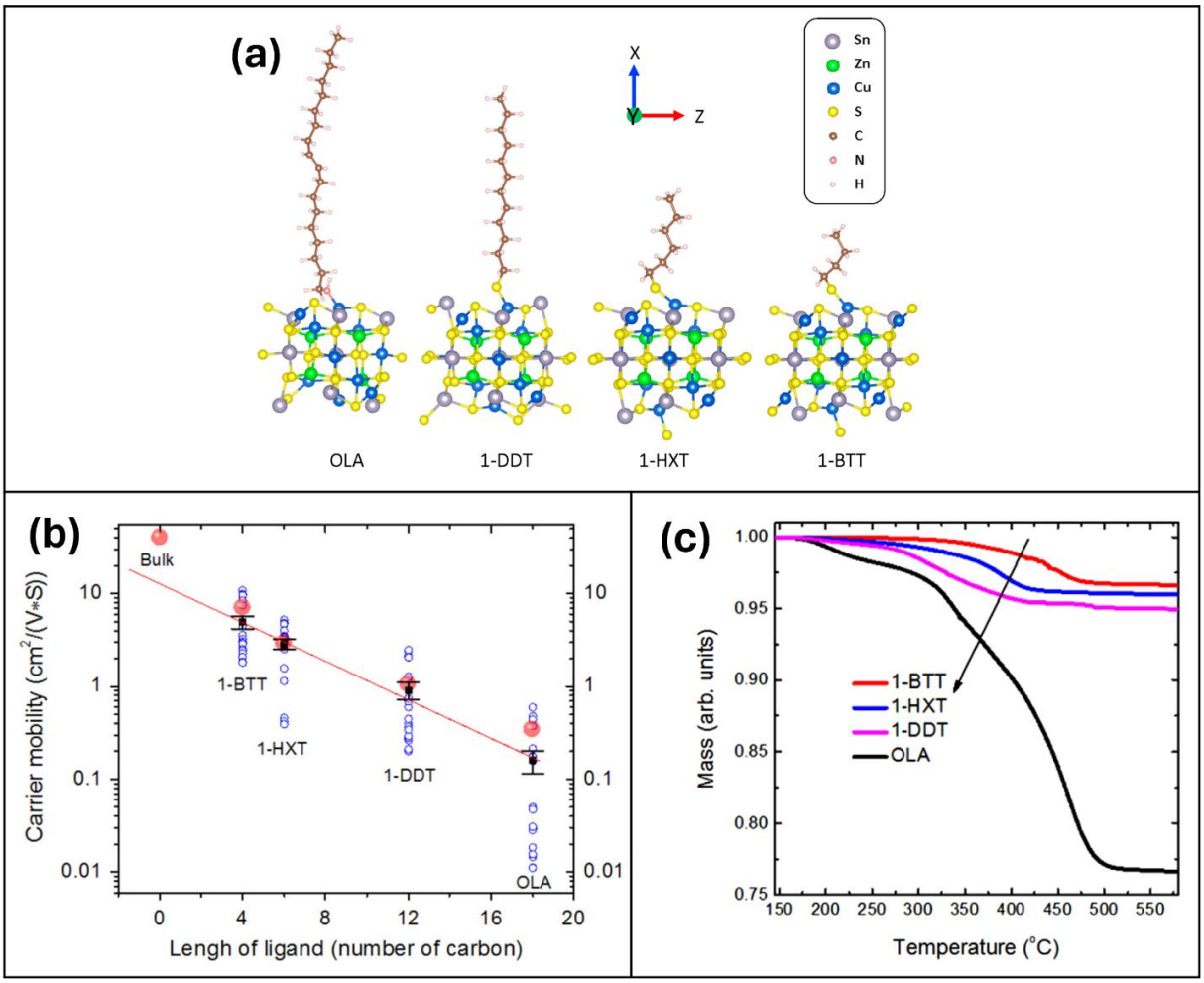

Figure 8. (a) CZTS lattice structures show the ligand lengths of multiple organic ligands used for the synthesis of nanocrystals (HXT=1-hexanethiol). (b) Plot depicting the effect of ligand chain length on the carrier mobility of nanocrystal. (c) TGA measurement reveals a higher mass loss of OLA ligands as compared to shorter ligands. Reproduced with permission.[214] 2014, Elsevier.

4.3. Grain Boundaries, Defects, and Recombination Sites

The excess of grain boundaries in finely grained nanocrystals can produce extra-recombination paths and can cause carrier trapping issues,[216] therefore, a selenization process (in combination with an annealing step) is crucial in enlarging the grains thereby minimizing the detrimental grain boundaries.[132,217] The increased grain boundaries in an FG layer would mean a higher surface area for CZTS particles which can increase the recombination probability. Guo et al. stated that the charge carriers generated in the unsintered (FG) layer cannot be efficiently collected at the contacts since they are quickly recombined in the FG layer itself.[90] This would decrease the external quantum efficiency (EQE) of the solar cell due to limited absorption of the photons since only an LG layer actively participates in

absorption. The primary reason behind annealing the precursor film is to minimize the detrimental grain boundaries such that the LG layer provides a sound platform for a workable PV device. This grain development is quite evident in the SEM images after annealing while the precursor films (before annealing) do not depict a layer that can effectively be used to conduct charge carriers owing to the richness in grain boundaries as shown in **Figure 9**. Miskin et al. found that the minimization of FG thickness enhanced the overall crystallinity of CZTS film, which led to a 25% increase in the PCE. This finding can be related to a decrease in recombination sites with an increased LG content which was achieved by optimizing annealing parameters.[146]

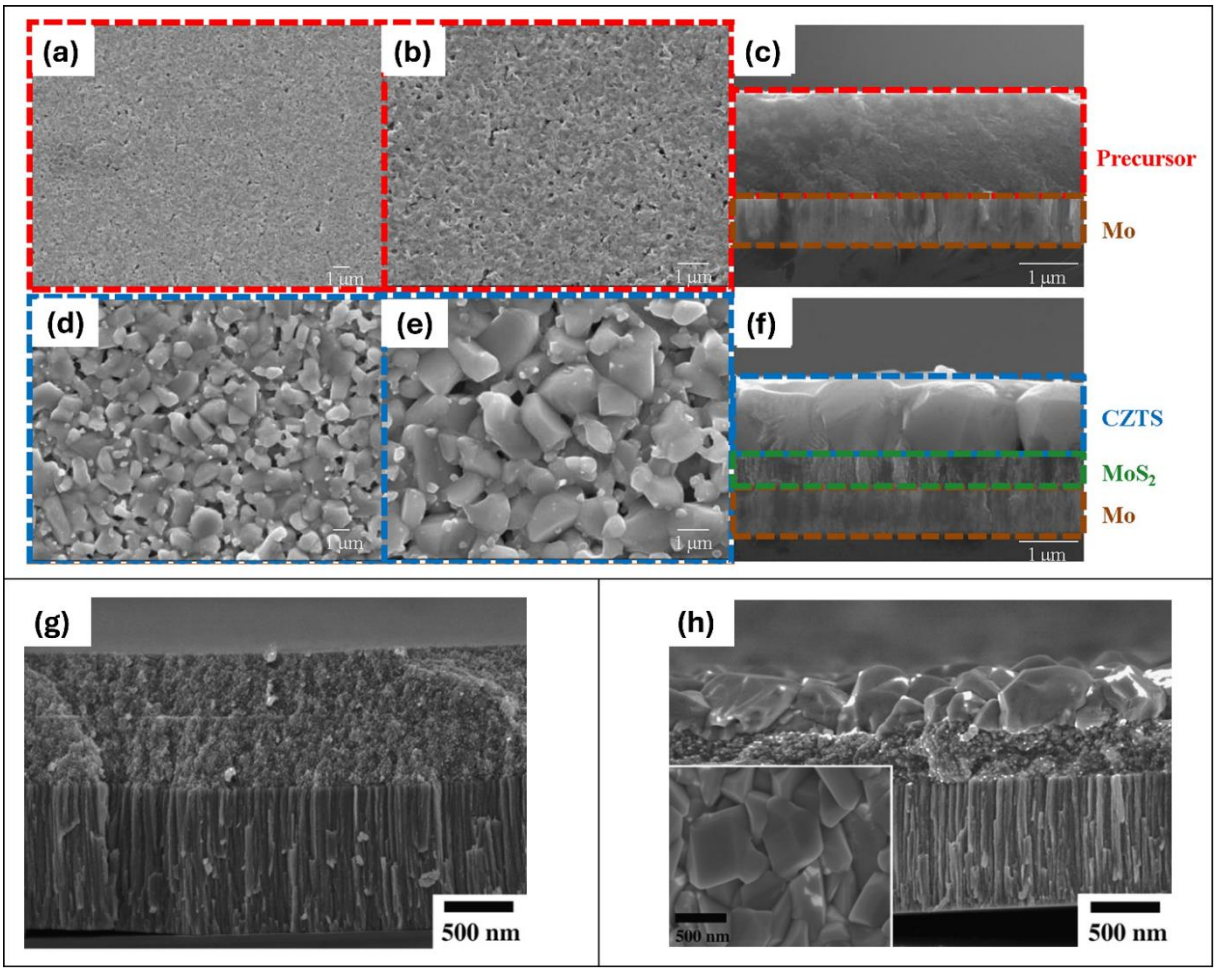

Figure 9. Surface and cross-sectional SEM images of the sequentially prepared (a–c) as-coated CZTS thin films, and (d–f) sulfurized CZTS thin films. Reproduced with permission.[218] 2016, Wiley. (g) CZTS precursor film without annealing, (h) CZTS bi-layer structure after annealing. Reproduced with permission.[90] 2012, Elsevier.

The inclusion of carbon in the crystal lattice of the kesterite phase can also introduce defects of different types. Experimentally quantifying the solar cell's dependency solely on the carbon-related defects has been a challenge, therefore, a few efforts have been made using simulation approaches to extract the influence of carbon-based defects on the electronic and optical properties of the kesterite layer.[122,200,201] Mutter et al. have extensively studied the carbon-based defect formation in kesterite crystals through a simulated modeling approach. Their calculations revealed that carbon double antisite defect complexes are expected in carbon-rich kesterite layers. However, these defects compensate for charges and do not contribute significantly towards bringing the efficiency of the solar cell down. The uncompensated charge defects have been reported to have too high formation energies and do not exist at a considerable concentration.[201]

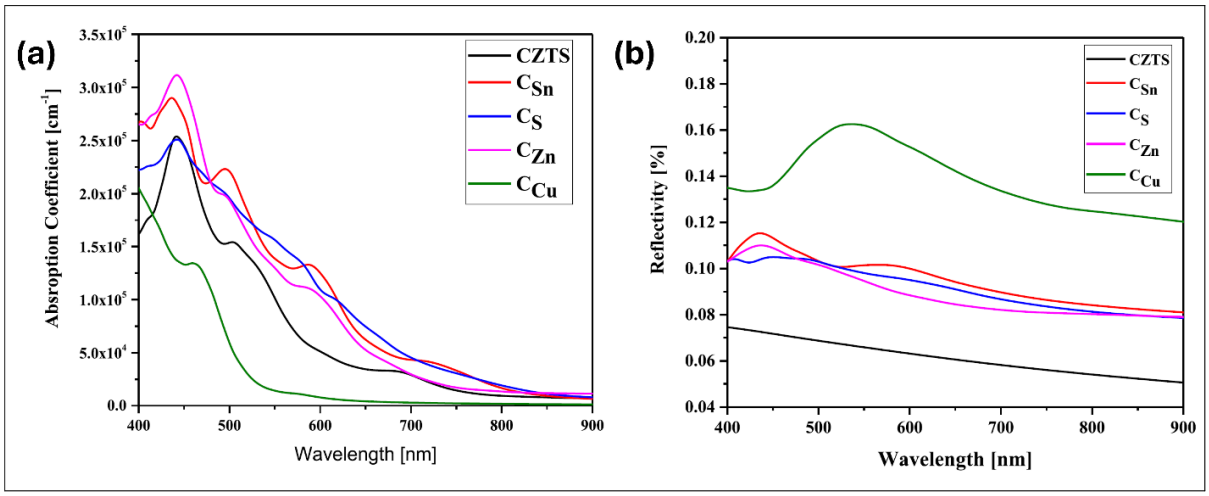

Figure 10. Comparison between (a) absorption coefficients and (b) reflectivity of different carbon antisites defects and CZTS model over a wavelength range. Reproduced with permission.[200] 2020, Elsevier.

Ahmoum et al. carried out density functional theory (DFT) calculations based on generalized gradient approximation to study the alteration in the electronic and structural properties of the CZTS model after the occupation of carbon atoms at various sites in the kesterite crystal lattice. Except for C_{Cu} defects, it was found in their calculations that the rest of the antisite defects increase the absorption coefficient as compared to the CZTS model as shown in **Figure 10(a)**. The substitution of carbon atoms at copper sites leads to an increase in the optical band gap as fewer electrons would occupy the density of states at the valence band maximum (previously occupied by 3d-Cu states). In the case of C_S and C_{Sn}, the increase in absorption coefficient even beyond 800 nm, is attributed to the existence of acceptor states

above the valence band. C_{Cu} defects also resulted in the highest reflectivity as compared to other C antisite defects while the CZTS model exhibited the lowest reflectivity as shown in **Figure 10(b)**. Furthermore, with the C_{Cu} defects, the valence band maxima became flatter indicating a higher mass of holes which resulted in poorer transport properties of the crystal lattice. The optical and electronic bandgaps remained almost similar after the substitution of carbon with sulfur atoms. The antisite carbon defect in place of sulfur formed a shallow acceptor level since the carbon atom donates two holes. The incorporation of carbon atoms at the Sn sites resulted in higher optical and electronic bandgap. The lesser atomic radii of carbon atoms as compared to Sn atoms caused a structural distortion. Moreover, this defect also led to the formation of a shallow acceptor level above the Fermi level. Acceptor states in the bandgap were not noticed in the case of C_{Zn} defects as Zn and C atoms possess the same number of valence electrons, hence, carbon replacing zinc can form a strong bond with sulfur atoms. Finally, it was concluded in their work that the photogeneration of charge carriers was improved under visible light excitation due to an increase in the density of states in the valence band. However, the impurity band in the bandgap can act as a recombination center by scattering the excited electrons. The intra-band defects can negatively influence the V_{oc} and FF by enhancing the Shockley-Read-Hall recombination and decreasing mobility.[200]

4.4. Occupation of Secondary Phases

The composition of kesterite crystals can be highly influenced by the incorporation of carbon impurities. It has been suggested that the nanocrystals at the FG layer are poor in cation content as the cations would diffuse out from the bottom side to the top grains and take part in the grain enlargement process during annealing.[114,120,121,187] This would result in a varied composition over the bi-layer structure which would eventually lower the quality of the film. Moreover, the FG layer being rich in the C-Se phase and poor in the CZTS phase indicates the occupation of secondary phases which can be a factor in lowering the PCE of solar cells.[120,123] The junction between the FG layer and $MoSe_2$ at the rear side can be a cause for efficiency losses in CZTS devices. $MoSe_2$ is formed as a result of the annealing treatment of absorber film which triggers Se diffusion into the Mo layer. Due to the existence of secondary phases near the junction between CRFG and back contact, band alignment issues can also arise. Campbell et al. used a combination of OLA and FA-processed CZTS films in a single device and reported that such a dual-layer structure outperforms CZTS films prepared with OLA solution alone. Since an FA molecule contains only one carbon atom (**Table 2**), the CZTS-FA film did not exhibit a CRFG layer at the back contact that offered a lower barrier

height with $MoSe_2$ and Mo contact while CZTS-OLA being high in quality in terms of less porosity was deposited on the top side thereby sandwiching the FG layer (accompanied with CZTS-OLA) in between the two types of CZTS layers (OLA and FA).[174]

5. Strategies to Exchange/Strip/Avoid Carbon-Rich Ligands in Nanocrystal Films

5.1. Ligand Exchange

As mentioned earlier, the formation of an FG layer beneath larger grains noticed after annealing is a consequence of organic residue occupation at the rear side of a solution-processed nanocrystal film. During annealing, the long aliphatic carbon chains (accompanied by carbon-rich solvent molecules) undergo decomposition and leave organic residues around nanocrystal surfaces that insulate nanoparticles which can hinder PV activities. Fortunately, the native carbon-rich ligands coordinated with the cationic sites of nanocrystal surfaces can be replaced with either shorter organic ligands having fewer carbon atoms or with inorganic ligands (virtually no carbon) in a chemical technique known as the "ligand exchange process".[214] The replaced inorganic ligands or shorter organic ligands can decrease inter-particle distances and provide a favorable environment for grain enlargement. In the case of amine-related ligands, the interaction between a ligand molecule and nanocrystal surface is developed due to the ability of the nitrogen atom (from the amine ligand) to share its lone pair of electrons with the cationic site of the nanocrystal surface. During a ligand exchanging event, the higher affinity of new ligand molecules to form a bond with the cationic sites of the nanocrystal forces the dissociation of native (carbon-rich) ligands from the nanocrystal surface. The ligand exchange process is facilitated by the nucleophilicity of incoming ligand anions and the electrophilic nature of uncoordinated metal ions on the nanocrystal surface as shown in **Figure 12** for different cases mentioned in the literature.

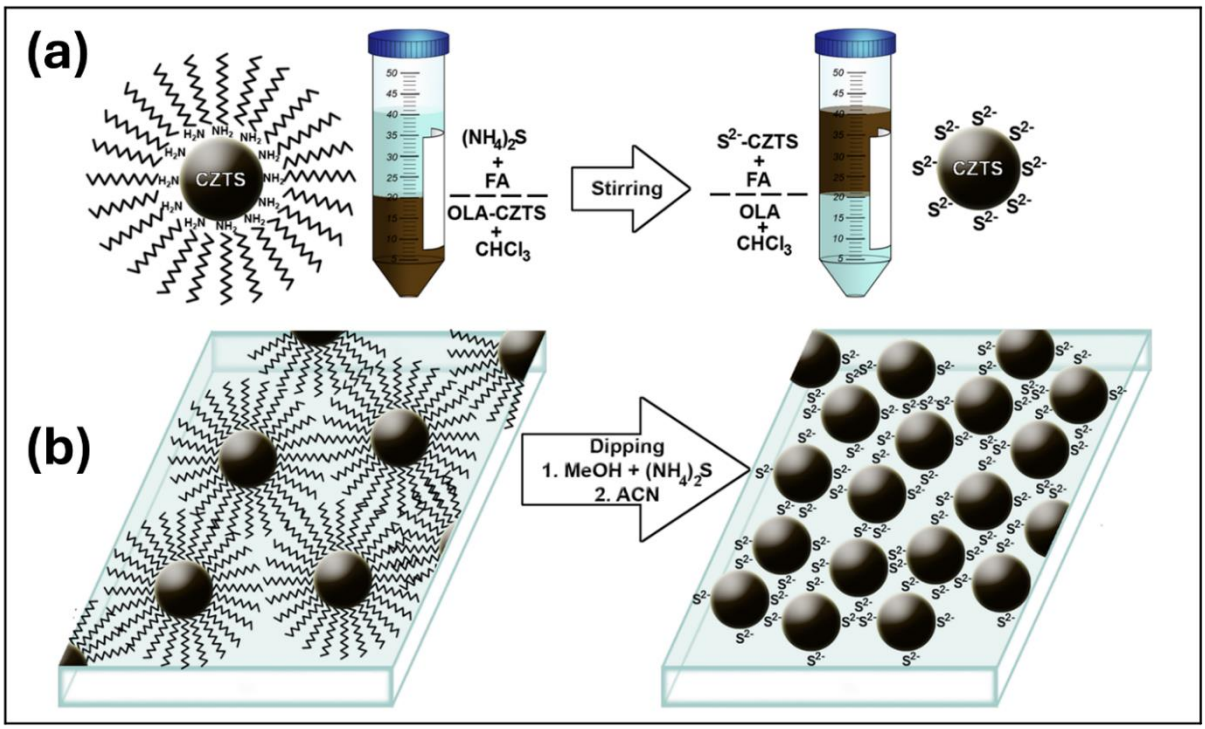

Figure 11. Illustration of (a) solution-phase ligand exchange representing a biphasic mixture to extract CZTS nanocrystals from a non-polar $CHCl_3$ solvent and (b) solid-phase ligand exchange showing the replacement of organic ligands with S^{2-} ions through the dipping process. Reproduced with permission.[219] 2017, American Chemical Society.

The success of a ligand exchange process is often characterized by TGA and Fourier transform infrared spectroscopy (FTIR) measurements by various works as shown in **Figure 13**. A strong IR signal existing around 2800-3200 cm^{-1} is indicative of C-H related peaks and is featured in nanocrystals covered with carbon-rich organic ligands.[204,205,220] In TGA measurements, the mass loss of nanoparticles at high temperatures is measured where nanoparticles coordinated with long and bulky ligands show a higher mass loss. A good merit of a decent ligand exchange process is that while it should completely remove native ligands from the nanocrystal surface, it should not change the composition of the nanocrystal by over-etching the surface. The ligand exchange procedure can be conducted using both solution-phase and solid-phase approaches as presented in the schematic shown in **Figure 11(a)**. In a typical solution-phase ligand exchange process, a biphasic liquid mixture is created in which one part contains the dissolution of carbon-rich ligand-capped nanocrystals ink in a non-polar solvent, and the other part contains the ligand exchange agent diluted in a polar solvent. As a result of vigorous shaking/stirring for an extended period, the nanocrystals would be extracted by the polar solvent where shorter organic ligands replace the longer ones. For a solid-phase exchange process, the reaction takes place after the nanocrystals are deposited in the form of a

film onto a substrate. A solution containing the ligand exchange agent is dropped onto the deposited film which soaks the chemical and the exchange reaction occurs between solid-phase nanocrystals and etchant molecules **(Figure 11(b))**. Alternatively, the film can be dipped into chemical solutions to execute the ligand exchange process. As shown in **Table 4**, both processes have been widely used for ligand exchange procedures, however, our literature study suggests that the liquid-phase method has been a popular choice.

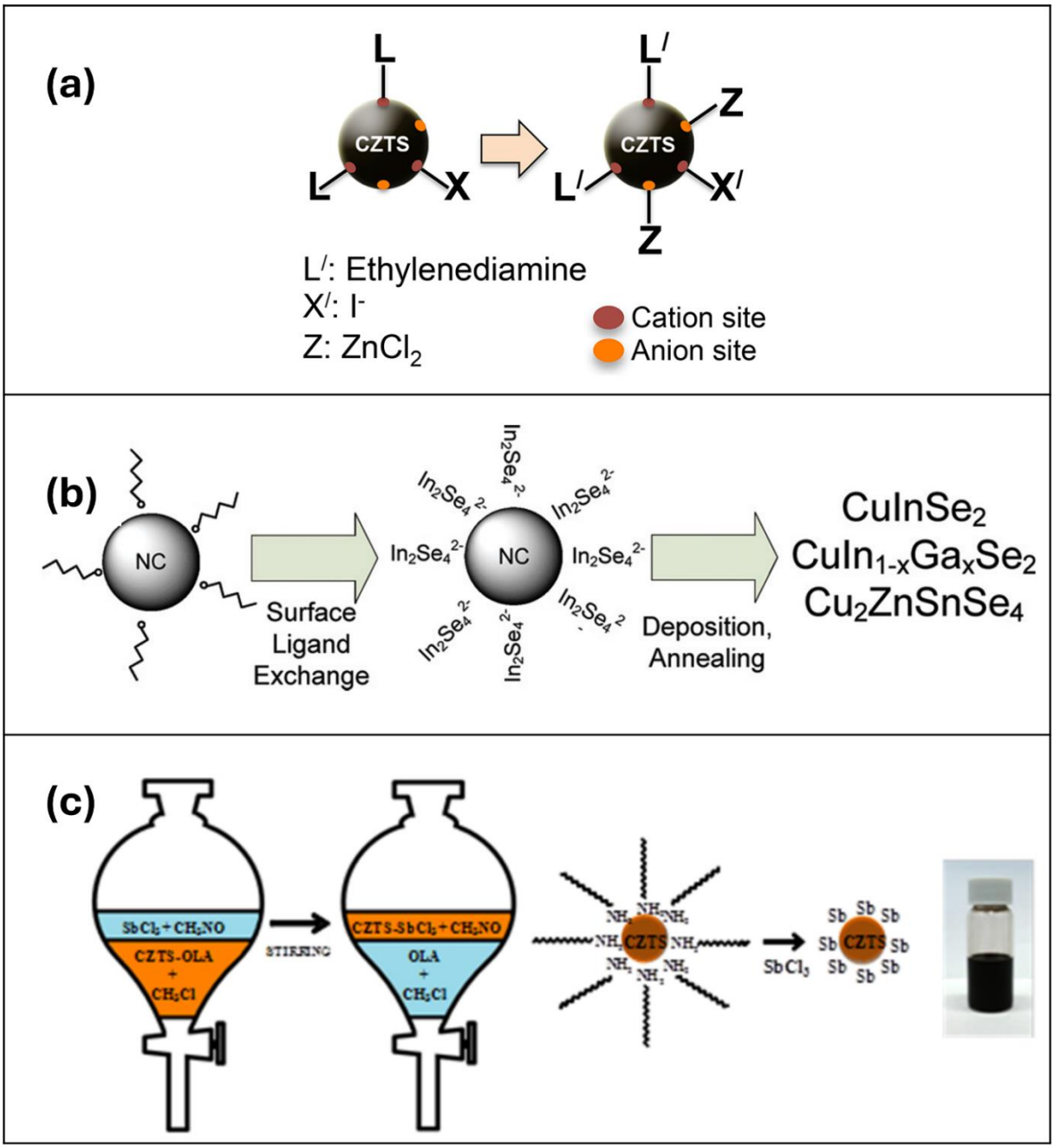

Figure 12. (a) Schematic of Korala et al. work to replace the long OLA-based ligands represented by L with shorter EDA ligands represented by L' at the cationic site of the nanocrystals whereas the anionic sites represented by X are replaced with I^- ions and

passivated with $ZnCl_2$. Reproduced with permission.[219] 2017, American Chemical Society. (b) Schematic of surface ligand exchange process showing $In_2Se_4^{2-}$ ions replacing organic ligands bonded with nanocrystal. Reproduced with permission.[221] 2012, American Chemical Society. (c) Schematic representation of solution-phase ligand exchange process used for replacing OLA ligands from CZTS nanocrystals with inorganic $SbCl_3$ ligands. Reproduced with permission.[206] 2013, American Chemical Society.

5.1.1. Shorter Organic Ligand Exchange Agents

Organic ligands possess excellent properties to serve as a capping agent which provides impressive colloidal stability and dispersibility to the nanoparticles.[222] However, it can become a problem in PV applications in which the long carbon tails of organic ligands hinder the electronic communication between nanoparticles. Therefore, the replacement of long organic ligands with shorter organic ligands from the nanoparticle surfaces is thought to be a favorable exchange strategy such that it keeps nanoparticles from forming agglomerates through steric repulsion and meanwhile decreases the inter-particle distance for better electronic coupling as well. Several organic ligand exchange chemicals, including EDA,[219] EDT,[208] pyridine,[215] and 5-amino-1-pentanol (AP),[118] have been employed to replace native bulky organic ligands from CZTS nanocrystal surface. Gong et al. adopted an OLA-based solvothermal approach to synthesize the CZTS absorber layer. They opted for a solid phase ligand exchange process in which EDT was selected as the shorter ligand to replace the long OLA ligands. In their synthesis method, a colloidal solution containing the metallic precursors in OLA and OLE was heated in a Teflon-lined stainless-steel autoclave. The prepared CZTS ink was spin-coated onto a Si substrate to develop a 500 nm thick absorber layer. The ligand exchange process was carried out by treating the deposited film with a 0.1 M solution of EDT dissolved in acetonitrile (MeCN). The film was soaked in the ligand exchange agent for 3 mins where the nucleophilic molecules of EDT would attack the cationic sites of the nanocrystal surface and force the desorption of OLA molecules. After the successful replacement of long and bulky OLA-based ligands with shorter EDT ligands, the decrease in inter-particle distance allowed better conduction which was evidenced by 5 times higher PCE of the EDT-CZTS device as compared to the OLA-CZTS solar cell. An after-effect of ligand-exchanged nanocrystals was noticed in SEM images which revealed the formation of cracks due to nanocrystals moving closer to each other.[208] Embden et al. reported a facile ligand exchange strategy to replace OLA/DDT ligands from CZTS nanocrystals with shorter AP ligands. Their findings revealed a 96% reduction in the IR C-H

signal when long OLA/DDT ligands were replaced with shorter AP ligands. A complete volatilization of AP ligands was found at 350°C as TGA measurement revealed no mass loss beyond this temperature. The PCE of ligand-exchanged CZTS nanocrystal solar cells was noticed to be improved.[118] Saha et al. utilized a solid-phase ligand exchange approach to displace OLA ligands from CZTS nanocrystals with pyridine ligands having shorter carbon chains. In their solid phase exchange process, a series of spin-coating steps were conducted to effectively replace carbon-rich OLA chains with pyridine ligands. Initially, OLA-capped CZTS nanocrystal ink was deposited onto the ITO substrate followed by dropping pyridine solution onto the film to execute the ligand exchange process. Subsequently, MeCN and toluene were spun as part of the washing step.[215] Semalti et al. tried a post-synthesis liquid-phase ligand exchange process on TOPO-capped CZTS nanocrystals with butylamine, however, the decomposition of the kesterite phase into Cu_2S binary phases showed the incapability of butylamine to successfully exchange with native TOPO ligands while keeping the CZTS phase intact.[93]

5.1.2. Inorganic Ligand Exchange Agents

Like organic ligands, inorganic ligands provide the required repulsive interaction between nanoparticles to keep stabilization but also come with an added advantage that even after decomposition, they do not leave carbonaceous impurity between nanoparticles. Among inorganic ligands, antimony trichloride $SbCl_3$,[206] ammonium sulfide $(NH_4)_2S$,[223] and $(NH_4)_4Sn_6S_2$,[207] have shown effective ligand exchange properties with CZTS.

Inorganic metal chalcogenide complexes (MCC) can stabilize nanoparticles in a colloidal solution and possess the ability to provide decent electronic coupling between adjacent nanoparticle surfaces.[115,224] An MCC ligand is composed of a central metal group coordinated with a chalcogen anion that offers electrons for connection with the nanocrystal surface. Nanocrystals dispersed in MCC ligands have shown high carrier mobilities.[115] Hydrazine-stabilized MCC has been employed as a capping agent for the synthesis of many stable nanocrystals.[225] However, the toxicity of hydrazine has led to the development of MCC with environment-friendly solvents like H_2O, DMSO, or FA.[115] Kim et al. achieved a carbon-free composition of CZTGeS in which the native OLA ligands from the absorber layer were replaced with an MCC featuring $Sn_2S_6^{4-}$ ions. The solution-phase ligand exchange process was undertaken by reacting CZTGeS nanocrystals dissolved in hexane with $(NH_4)_4Sn_6S_2$ mixed in FA solvent. Successful ligand removal was depicted by both TGA and FTIR measurements. The ligand exchange procedure resulted in an increase in the PCE from

3.4% to 4.6%. A graded bandgap structure further increased the PCE to 6.3% wherein grading was achieved by tuning the Sn/Ge ratio. A higher adsorption of $Sn_6S_2^{4-}$ on the nanocrystal surface led to a decrease in the bandgap. The graded bandgap structure was achieved by varying adsorption of MCC ligands ($Sn_2S_6^{4-}$ ions) which was made possible by coating multiple layers of absorber film treated with varying concentrations of $(NH_4)_4Sn_6S_2$.[207] However, the presence of a metal group in MCC can affect the physical and chemical properties of the nanocrystal it is coordinated with, for instance, the multivalent nature of Sn can influence $Sn_2S_6^{4-}$ to participate in a redox reaction.[226] Such a complication can be circumvented by using metal-free inorganic ligands. For this purpose, several metal-free inorganic complexes have been explored as effective ligand exchange agents, such as chalcogenides (S^{2-}, Se^{2-}, and Te^{2-}), hydro chalcogenides (HS^-, and HSe^-), and mixed chalcogenide (TeS_3^{2-})[226]

Compounds containing S^{2-} ions (e.g. $(NH_4)_2S$)) have proven to be effective inorganic ligand exchange agents given the nucleophilicity of S^{2-} ions to develop a strong interaction with metallic groups at the nanocrystal surface. The effectiveness of S^{2-} to replace OLA/DDT ligands from CZTS nanocrystal has been validated by Zhang et al.[227] They adopted a solution-phase ligand exchange method in which $(NH_4)_2S$ dissolved in FA was mixed with OLA/DDT-capped CZTS nanocrystals dispersed in toluene to create an immiscible mixture. After constant stirring for 2 hrs, the CZTS nanocrystals shifted to the polar phase. The disappearance of IR signal at 2858 cm^{-1} and 2921 cm^{-1} for ligand-exchanged nanocrystals showed the success of their process while the unchanged XRD spectra confirmed the preservation of nanocrystals after the solution-phase ligand exchange process. Furthermore, higher absorption of S^{2-} capped CZTS nanocrystals (dispersed in methanol) can be explained by strong mechanical coupling energy as nanocrystals became closer to each other after the solution-phase treatment. Mary et al. have also used a similar solution-phase approach in their work to exchange long OLA ligands from CZTS nanocrystals (prepared with the hot injection method) with S^{2-} ligands. They reported that the hydrophobic OLA-CZTS nanocrystals were converted into hydrophilic S^{2-}-capped nanocrystals after the ligand exchange process which was verified by the dispersion of ligand-exchanged nanocrystals in polar solvents like water and ethanol.[223] The same research group showed the competency of a solid-state ligand exchange approach via a dip coating method using the same $(NH_4)_2S$ chemical. A solution of $(NH_4)_2S$ diluted in methanol was prepared as a ligand exchange chemical. Oleate-capped CZTS nanocrystal film was dipped in ligand exchange chemical for 30 secs followed by dipping in methanol to remove unbounded inorganic salt molecules around nanocrystals. The

layer-by-layer deposition was done multiple times to achieve the desired thickness of S^{2-} capped nanocrystals. Like the solution-phase process, the solid-phase ligand exchange also resulted in the elimination of C-H peaks from the IR spectra of the S^{2-} capped nanocrystal. Moreover, compared to the 25% mass loss of OLA-capped nanocrystals at 500^{o}C, the mass loss of ligand-exchanged nanocrystals was just about 8%. The crystal structure and phase of the CZTS nanocrystal remained intact after the solid-state ligand exchange process as evidenced by XRD and Raman results.[228] Apart from these works, several other works have also opted $(NH_4)_2S$ as a viable ligand exchange agent due to its ability to provide electrostatic stabilization between polar solvents and nanoparticles as shown in **Table. 4**.[168,219,227–229]

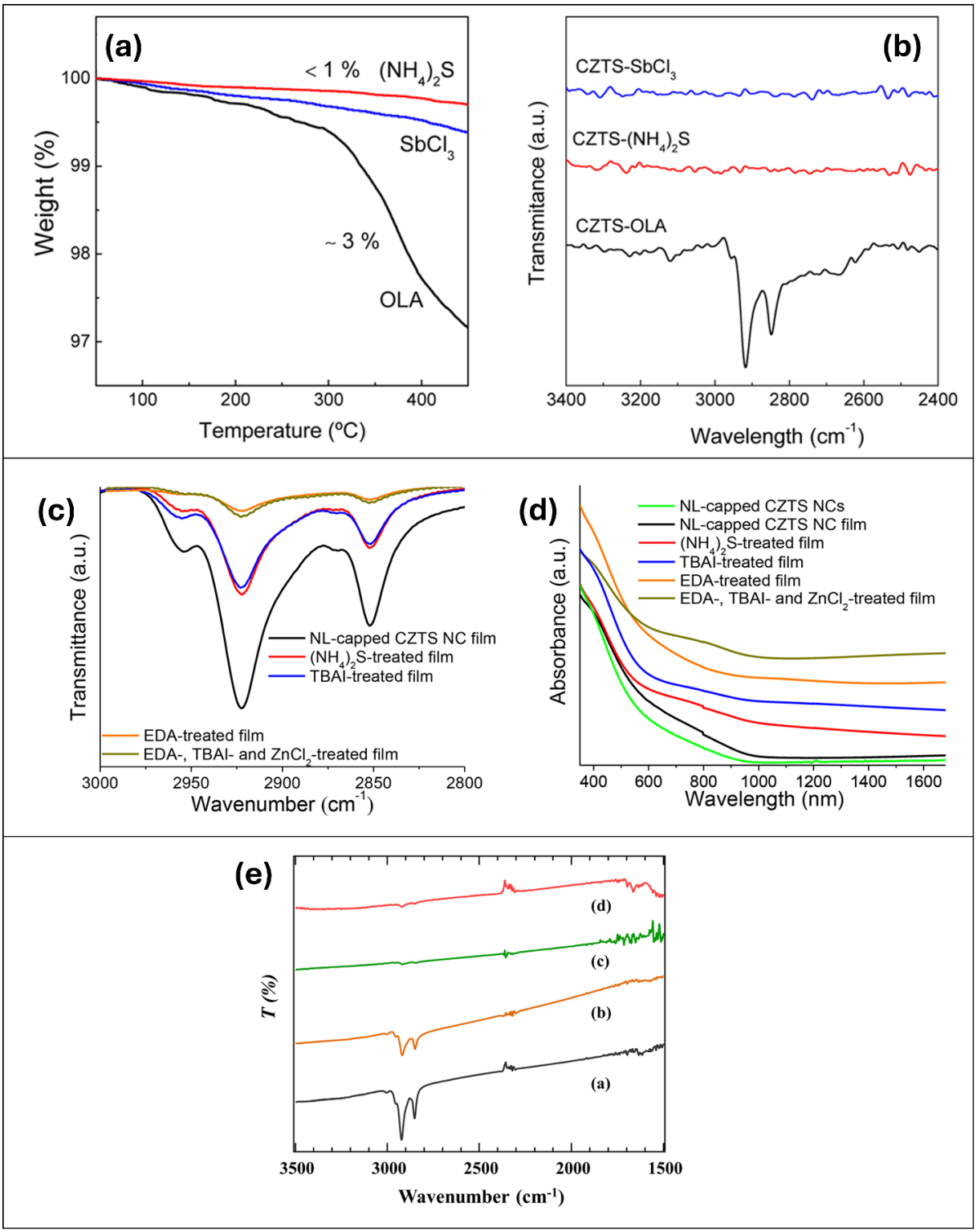

Figure 13. (a) TGA and (b) FTIR spectra from CZTS-OLA, CZTS-$SbCl_3$, and CZTS-$(NH_4)_2S$ nanoparticles. Reproduced with permission.[206] 2013, American Chemical Society. (c) FT-IR spectra of CZTS NC films and (d) UV−vis−NIR spectra of CZTS nanocrystal films. Reproduced with permission.[219] 2017, American Chemical Society. (e) FT-IR spectra of thin films of CZTS nanocrystals for as-synthesized and following treatment with EDT, $(C_2H_5)_3OBF_4$, and CH_3I. Reproduced with permission.[204] 2014, American Chemical Society.

Antimony-based ligands also hold the potential to be used in an inorganic ligand exchange process. Carette et al. used $SbCl_3$ salts to displace the OLA ligands from the CZTSe nanocrystal surface with Sb ions. The colloidal nanoparticles of Cu, Zn, and Sn were dispersed in OLA and octadecyl-phosphonic acid (ODPA) solution. OLA contributed towards controlling the nanoparticles' growth and maintaining their stability while ODPA was responsible for managing the composition of nanocrystals. While ODPA mostly evaporated during the annealing step, OLA ligands decomposed and left carbon residues which formed a bi-layer structure in the final deposited film. Hence, to remove the formation of an FG layer, the OLA ligands were displaced with inorganic $SbCl_3$ salt molecules before the thermal treatment required for selenization. As shown in the schematic in **Figure 12(c)**, the ligands were displaced by reacting to the nanoparticles dissolved in chloroform with 0.1M $SbCl_3$ in FA which gave rise to a biphasic solution. The solution was shaken vigorously until the nanoparticles were extracted to the FA phase where they reacted with $SbCl_3$ salt and OLA ligands were successfully displaced with Sb ions. Subsequently, the FA solution containing the ligand-exchanged nanoparticles was washed with DMF and MeCN to eliminate the impurities. The success of this ligand exchange strategy was confirmed from FTIR spectra where the C-H signal was seen to be mostly eliminated as shown in **Figure 13(b)**. Furthermore, the bulky ligand nature of CZTSe-OLA nanocrystals was evidenced by a mass loss of 3% after annealing it at 450^{o}C while CZTSe-Sb nanocrystals exhibited a mass loss of even less than 1% at the same annealing conditions as shown in **Figure 13(a)**. Moreover, $SbCl_3$ not only helped in ligand exchange but also made a conducive environment for better crystallization. They have also mentioned the complete evaporation of Sb after annealing for 1 hr as measured by XPS and EDS analysis.[206]

5.1.3. Hybrid (Organic-Inorganic) Ligand Exchange Agents

Organic ligands have been known to provide decent dispersibility and stability in a colloidal nanocrystal solution while inorganic ligands come with the advantage of having zero carbon thereby not forming potentially detrimental carbonaceous residues upon decomposition during thermal treatment. The effectiveness of both organic and inorganic ligands to successfully replace native ligands has been shown in previous sections. However, it is difficult to conclude which ligand type holds the upper hand in terms of higher PV performance since the efficiency of a kesterite solar cell is influenced by other factors as well, such as defect formation in bulk, interface properties with buffer, and the presence of secondary phases.[30]

To address the issues related to incomplete ligand removal, poor colloidal stability, and over-etching of nanocrystal surface, a hybrid ligand exchange approach involving both inorganic and organic ligands has been proposed in literature where both ligand types are expected to complement each other to enhance properties of ligand exchanged nanocrystals.[168,219] Elis et al. adopted this hybrid ligand exchange strategy on OLA-capped CIGS nanocrystals prepared with a microwave-assisted solvothermal method. The nanocrystals were first replaced with pyridine ligands as an organic ligand exchange step followed by treatment with $(NH_4)_2S$ to exchange the remaining native ligands with inorganic S^{2-} ions. This strategy led to an impressive 98% removal of native ligands and increased the PCE from 9.2% to 12%.[168] Korala et al. conducted a hybrid ligand exchange process on OLA-capped CZTS nanocrystals and investigated the ability of $(NH_4)_2S$, tetrabutylammonium iodide (TBAI), and EDA to passivate nanocrystal surface. The OLA-CZTS nanocrystals were coated on a glass substrate using the drop-casting method and then dipped into multiple chemicals to execute ligand exchange. It was found that native OLA ligands coordinated with the cationic sites of CZTS nanocrystals were replaced with shorter EDA ligands and inorganic ligands (S^{2-} or I^-) as shown in **Figure 12(a)**. This treatment resulted in a 90% decrease in the intensity of the C-H stretching peak. Moreover, the anionic sites on the surface of nanocrystals were passivated with Zn^+ ions by reacting the nanocrystals with $ZnCl_2$. Hall measurements taken on the ligand-exchanged CZTS nanocrystals exhibited an increase in conductivity (9.4×10^{-3} S cm^{-1}), and charge carrier concentration (3.3×10^{17} cm^{-3}) which consequently led to an improvement in the V_{oc}.[219] **Table 4** categorizes different works that have adopted ligand exchange strategies.

Table 4. List of ligand exchange strategies used by various works to replace organic ligands with shorter organic, inorganic, and hybrid ligand exchange agents.

Ref	Absorber Layer	Synthesis Method	Native Ligands	LE Type	LE Agent	LE Process	Year
[215]	CZTS	Hot Injection	OLA/DDT	Organic	Pyridine	Solid Phase	2012
[229]	CZTSe	Hot Injection	OLE	Inorganic	$(NH_4)_4S_2$	Liquid Phase	2022
[207]	CZTGS	Hot Injection	OLA	Inorganic	$(NH_4)_4Sn_2S_6$	Liquid Phase	2014
[206]	CZTSe	Pulsed Spray	OLA/ODPA	Inorganic	$SbCl_3$	Liquid Phase	2013

[208]	CZTS	Solvothermal	OLA	Organic	EDT	Liquid Phase	2016
[230]	CZTS	One-Pot Heat	OLA	Hybrid	EDA/$(NH_4)_4S_2$	Solid Phase	2018
[118]	CZTS	Hot Injection	OLA/DDT	Organic	AP	Liquid Phase	2014
[227]	CZTS	Hot Injection	OLA/DDT	Inorganic	$(NH_4)_2S$	Liquid Phase	2015
[223]	CZTS	Hot Injection	OLA/OLE	Inorganic	$(NH_4)_2S$	Liquid Phase	2022
[228]	CZTS	Hot Injection	OLA	Inorganic	$(NH_4)_2S$	Solid Phase	2020
[168]	CIGS	Solvothermal	OLA	Hybrid	Pyridine/$(NH_4)_2S$	Liquid Phase	2020
[219]	CZTS	Hot Injection	OLA	Hybrid	$(NH_4)_2S$/TBAI/EDA	Solid Phase	2017

5.2. Ligand Stripping

Contrary to ligand exchange agents, trialkyl oxonium salts have been known to completely remove the ligands from the nanocrystal surface and the technique is termed as ligand stripping.[205,220,231] The alkylating activity of ligand-stripping agents would break the coordination complex between metal ions from nanocrystals and nucleophilic ligands.[220] For semiconductor applications, a ligand stripping strategy can be more desirable (than ligand exchange) since it completely removes the native ligands from nanocrystal surfaces. However, the success of this process is highly dependent on the nature of ligands and the interaction between the etchant and the nano-dispersive ink.

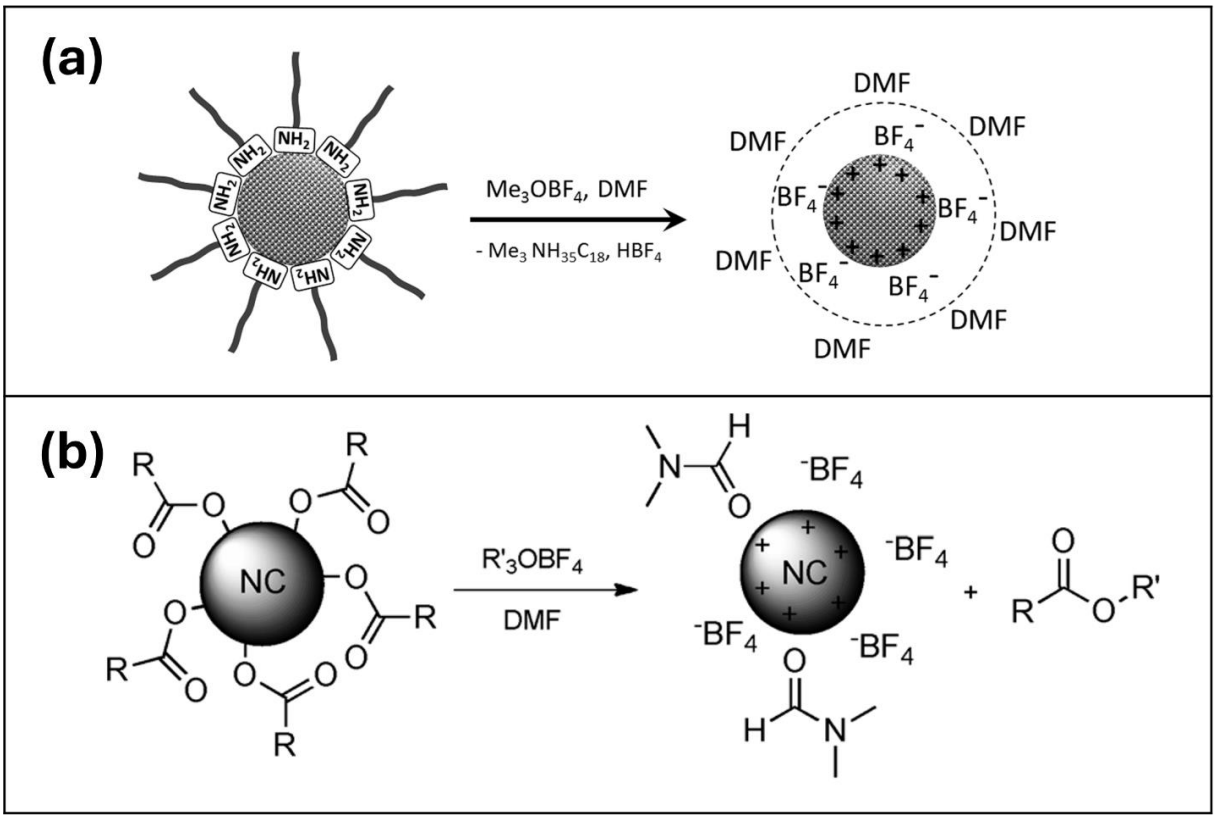

Figure 14. (a) Schematic representation of the OLA ligand stripping from CZTS nanocrystals with Me_3OBF_4 treatment. Reproduced with permission.[205] 2016, Wiley. (b) Reactive ligand stripping of amine-passivated nanocrystals with trialkyl oxonium salts. Reproduced with permission.[220] 2011, Wiley.

Rosen et al. put forward the idea of ligand stripping using triethyl-oxonium tetrafluoroborate ($(C_2H_5)_3OBF_4$) or (Et_3OBF_4) also known as "Meerwein's reagent" to perform the alkylating activity on nanocrystals covered with carbon-rich ligands as shown in **Figure 14(b)**. The complete removal of oleate-based native ligands from the surface of the PbSe nanocrystal was demonstrated. Meerwein's reagent was selected as a suitable etchant since being a trialkyl oxonium salt, it offers ligand stripping while keeping the physical and crystal properties of the subjected nanocrystal intact. PbSe films prepared on Si substrate were immersed in Meerwein's reagent diluted in MeCN for 5 mins followed by excessive washing with MeCN and hexane to ensure ligand removal. The efficient removal of oleate ligands was confirmed through FTIR and EDS measurements taken post-chemical treatment. The performance of ligand-stripped PbSe was observed to be improved in terms of higher conductivity.[220] Suehiro et al. used the alkylating nature of Meerwein's reagent and methyl iodide (CH_3I) to strip the native OLA-based ligands from the surface of CZTS nanocrystals. The spin-coated CZTS nanocrystal films were dipped into 100 mM of Meerwein's reagent (diluted with 10

mL of MeCN) for 5 mins. After the film was taken out, it was washed in a DMF + MeCN (1M+10mL) solution and subsequently cleaned with hexane for several mins. The native OLA ligands previously present in the form of primary amines were converted into loosely bonded quaternary amines after the ligand stripping process and were ultimately washed away by DMF solution. The elimination of native ligands was first evidenced by the insolubility of CZTS nanocrystals in hexane and then confirmed by the removal of C-H peaks around 2900 cm^{-1} noticed in FTIR spectra taken post-chemical treatment. Finally, compared to no PV response generated from the OLA-CZTS device, a PCE of 0.05% exhibited the photoconductivity of ligand-stripped CZTS nanocrystals.[231] Khanzada et al. adopted the same strategy for the complete removal of OLA-based ligands from CZTS nanocrystals prepared by hot injection nanoparticle synthesis. The alkylating activity of Meerwein's reagent caused the breakage of the bond between the CZTS surface and the OLA ligand as shown in **Figure 14(a)**. After the removal of OLA ligands, the positively charged surface of the nanocrystal is stabilized by the presence of weakly coordinating BF_4^- ions which were removed from the nanocrystal vicinity through DMF washing and eventually resulted in a ligand-stripped CZTS nanocrystal. The stripping of OLA ligands was confirmed when nanocrystals were seen flocculating between a biphasic mixture of hexane and MeCN containing Meerwein reagent (termed as Me_3OBF_4 in **Figure 14(a)**) after shaking a few times. The optical absorbance response of the ligand-stripped nanocrystals measured by the UV-vis technique was noticed to be identical to OLA-CZTS nanocrystals evidencing the feasibility of chemicals used for ligand removal and viability of ligand-stripped nanocrystals for the PV application. However, a transmission electron microscopy (TEM) showed the average nanocrystal size decreased from 5.45 ± 1.5 nm to 5.15 ± 1 nm after the ligand removal process, this small reduction in the nanocrystals' size suggested slight over-etching of the nanocrystals' surface during the ligand removal process. A lower poly-dispersibility coefficient for ligand-stripped nanocrystals showed lesser inter-particle distances between nanocrystals which further confirmed the effectiveness of this technique. Moreover, XRD results showed that there were no additional phases after the ligand stripping process suggesting purity of kesterite nanocrystals. Although the FTIR peaks associated with C-H bonds significantly decreased after chemical treatment, complete removal of ligands encompassing CZTS nanocrystal was not claimed. The performance of ligand-stripped nanocrystals was seen to be improved in terms of higher photoconductivity and mobilities of both charge carriers.[205]

5.3. Ligand Exchange/Stripping Free Approach

Several researchers have opted for a ligand exchange(stripping)-free strategy to circumvent the additional chemical processing steps and cost required for the ligand exchange/stripping method meanwhile avoiding the existence of CRFG in the kesterite layer using carbon-poor, environment-friendly, and green solvents.[96,165,173,232,233] Huang et al. have claimed to introduce the first direct synthesis of CZTS nanocrystals in FA solvent thus precluding commonly used carbon-rich solvents (OLA, TOPO, OLE, etc.) thereby eliminating the occupation of long hydrocarbon chains on CZTS nanocrystals. FA was mixed with thioacetamide (TAA) to provide a stable dissolution to Cu, Zn, and Sn source compounds. Their reported TEM images showed dispersible CZTS nanoparticles with 5.2±1.2 nm sizes while no secondary phases were detected by XRD and Raman results. The presence of S^{2-} ions on the surface of nanocrystals during the synthesis process allowed their dispersibility and stability in polar solvents where TAA decomposition led to the formation of S^{2-} ions. Although FA offers less effective colloidal stability of nanocrystals, it does allow higher supersaturation of precursor salt as was mentioned in their report. Furthermore, carbon can vaporize by forming volatile compounds at a higher rate in FA-based nanocrystals as compared to OLA. The reported SEM images showed that the CZTS-FA nanocrystal film featured a single LG layer after annealing and the use of FA as a solvent effectively eliminated the CRFG layer thus obviating additional steps for ligand exchange/stripping. Moreover, as gathered by TGA measurements, a higher mass loss of 24.4% for CZTS-OLA nanocrystals compared to 8.7% for CZTS-FA nanocrystals at 500^{o}C exhibited the significantly lower bulky nature of FA-related ligands which is useful in creating a better inter-particle coupling.[96] Kush et al. offered a surfactant-free pathway to produce water-dispersible CZTS nanoparticles. In their method, the metal precursors and sulfides were mixed and stirred continuously in distilled water and later transferred to a hydrothermal flask and treated at 180^{o}C for 18 hrs to allow crystal growth and finally, the synthesized ink was dispersed in water, ethanol, and acetone. This strategy liberated the use of expensive and carbon-rich organic capping reagents, such as OLA and TOPO. It was found that such water-dispersible bare-surface nanocrystals were stable for more than a month and agglomerates formed after this period could be re-dispersed using sonication. The dispersive nature of this nanocrystal ink in solvents like water and ethanol made this method viable for producing low-resistive hydrophilic bare-surface nanocrystals. The complete absence of organic ligands from the nanocrystal surfaces not only obviated tedious ligand exchange/stripping steps but also made the prepared film independent of thermal treatments required for grain enlargement and

evaporation of carbon residues. The prepared bare-surface CZTS nanocrystal film offered a conducive environment for electrical conductivity and improved the inter-particle interaction leading to a lesser exciton recombination effect.[232] Ghropade et al. have used EG as an alternative green solvent to obviate the usage of carbon-rich solvents to synthesize CZTS nanocrystals. In their strategy, ethanol was used to disperse nanoparticles as a replacement for carbon-rich organic solvents used for the same purpose.[165] Wang et al. reported a 4.92% kesterite solar cell prepared with EG as the solvent to produce CZTS nanoparticles. However, their device featured an absorber film partially prepared with MEA to produce CZTS molecular ink. Nonetheless, the reported SEM images did not exhibit a distinctive CRFG layer.[233]

6. Our Perspective on the Impact of CRFG

Recently, a detailed compositional study of the CRFG layer was performed by our group.[234] The CZTSSe layer was synthesized by an OLA-based hot injection method. The CRFG layer presence was indicated by SEM images and EDS data. To conduct a precise compositional study, the CZTSSe layer was lifted off from the growth substrate using a rapid photonic lift-off (PLO) technique carried out with the help of a photonic curer. The cross-sectional structure of the CZTSSe solar cell and the PLO representation is given in **Figure 15(a)**. The successful lift-off of the CZTSSe layer was confirmed by the results gathered with XRD and Raman spectroscopy. As shown in **Figure 15(b)**, the rear side of the CZTSSe layer (rich in carbon) was subjected to XPS depth profiling analysis where argon ions (Ar^+) sputtering was used for removing portions of material from the surface. The elemental trends gathered from XPS spectra for different depths revealed a significant carbon content of almost 70% at the rear surface which decreased to less than 7% at the last measured depth (**Figure 15(c)**). On the other hand, the cation concentration was observed to be even less than 3% up to 35 mins of sputtering with Cu being completely absent (**Figure 15(e)**), hence this depth was referred to as the FG region. Upon increasing the sputtering time, the cation concentration increased to such values that suggested LG stoichiometry for the kesterite layer. Furthermore, the existence of carbon-rich ligands at the rear side of the absorber layer was confirmed by the attenuated total reflectance (ATR) spectrum which showed distinctive C-H peaks at 2800-3000 cm^{-1}, as shown in **Figure 15(d)**. Such a substantial difference between the elemental concentration of fine and LG layers alluded to the detrimental nature of the carbon-rich layer by introducing problems such as secondary phases, defect formation, bandgap fluctuations, and series resistance (due to poor metallic composition).

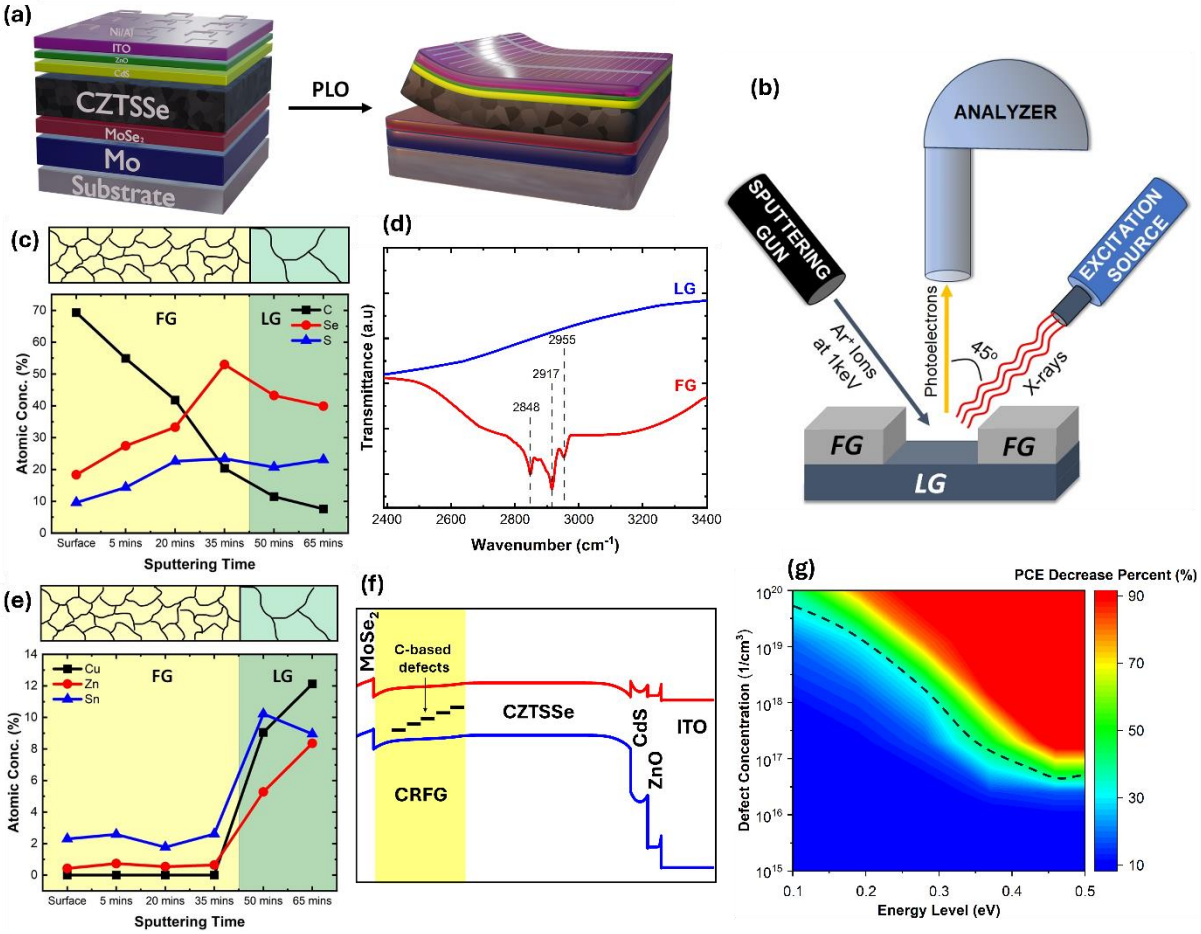

Figure 15. (a) Schematic of the cross-sectional structure of CZTSSe solar cell and the lift-off of the CZTSSe layer done by the PLO technique. (b) Schematic of XPS depth profiling used to study FG and LG compositions. (c) Content percent as a function of sputtering time extracted from fitted curves for C, S, and Se. (d) ATR results for FG and LG. (e) Content percent as a function of sputtering time extracted from fitted curves for Sn, Cu, and Zn. Reproduced with permission.[234] 2023, Wiley. (f) Band diagram of the simulated structure of CZTSSe solar cell containing CRFG with C-based defect model representing different energy levels used in the model. (g) Simulated PCE percent decrease (as compared to the CZTSSe solar cell without CRFG model) of the CRFG model with multiple defect concentrations and energy levels.

To put forward our perspective on the impact of carbon-rich layers on the electronic properties of kesterite solar cells, 1D diode simulations of the solar cell model are presented. The simulated CRFG defect models and their influences on the performance of the overall device have been discussed. It is expected that the presence of the CRFG layer contributes towards increased series resistance and the simulated result showed a gradual reduction in the

efficiency with an increased ratio of donor defect and deeper energy levels as depicted in **Figure 15(f)**. The parameters of the defect model of CRFG were adopted from Mutter et al.[201] Both acceptor-like and donor-like defects in the carbon-rich layer were considered in our SCAPS simulations to analyze the influence of such defects on the device's performance. However, it was found that acceptor-like defects do not cause any reduction in the simulated performance. To conduct a complete analysis of the donor-like defects, the defect density and energy levels varied between realistic ranges. It can be easily noticed in **Figure 15(g)** that the presence of donor-like defects is detrimental and causes a significant efficiency loss when defect density increases beyond 10^{17} cm^{-3}. Higher energy levels also become a crucial factor in curtailing efficiency since they are ascribed to deep defects. According to our simulations, a higher than 50% decrease in the PCE is noticeable after the dotted line in **Figure 15(g)** which shows that such combinations of defect density and energy levels cause serious efficiency losses. Therefore, the presence of a carbon-rich layer can potentially limit the device's performance by causing an increase in series resistance and introducing detrimental deep donor defects. A schematic of the C-based trap states existing in the CRFG layer is presented in **Figure 15(f)**, these defect states cause a significant decrease in the device's performance under the conditions seen in **Figure 15(g)**. Therefore, in the light of this detailed review study and investigations put forward according to our perspective, we have concluded that the explanations regarding the detrimental nature of the FG layer on the PV performance of the device seem more plausible and hence the different techniques for the removal of carbon-rich ligands presented in the fifth section can provide readers with relevant knowledge to target the CRFG layer removal from solution-processed kesterite layers. For future studies, we hope researchers in related fields cater to the important points raised by the extensive review study and perspective presented here on the CRFG layer in kesterite solar cells.

7. Summary

An extensive review of the existence and influence of CRFG in kesterite solar cells has been provided. Kesterite nanocrystal inks prepared with carbon-rich organic solvents almost inevitably result in the formation of a CRFG layer at the rear side of the annealed film. The decomposed bulky organic ligands composed of amorphous carbon residues hinder the grain growth process during annealing and give rise to a bi-layer structure composed of FG and LG sub-layers. There is not a unified consensus about the impact of such a layer on kesterite solar cell efficiency, however, given our detailed literature review, the reasons explaining the detrimental nature of CRFG seem more plausible. From our perspective, we have concluded

that the occupation of CRFG is deemed to adversely affect the solar cell performance in terms of enhancing series resistance, introducing detrimental carbon-based antisite defects, and causing the existence of secondary phases. Therefore, a detailed review of organic ligand-removing techniques presented here can benefit researchers targeting the elimination of carbon-rich layers from kesterite-based solar cells. Some of the important points of our literature study are summarized below:

1. Solution-based kesterite layers prepared with carbon-rich organic solvents feature a CRFG layer at the rear side of the absorber film.
2. OLA, TOPO, and OLE act as stabilizing ligands to the CZTS nanoparticles formed during the nucleation process often undertaken by a hot injection process.
3. Long aliphatic carbon chains cover the nanocrystal surfaces which arrest their growth and provide dispersibility and stability to the colloidal solution via steric repulsions.
4. An annealing step would allow the evaporation of organic content in the form of carbon-rich molecules from the nanocrystals' vicinity and elicit grain enlargement. The large micro-sized CZTS grains are deemed suitable for solar energy absorption and charge conversion.
5. The decomposition of organic ligands into randomly oriented amorphous carbon chains leaves residual organic impurities at the rear side of the absorber layer that hinder the grain enlargement process. This might happen because of; a. top LGs blocking the carbon-rich solvent molecules evaporation from the rear side, b. out diffusions of cations from bottom side grains, leaving behind the C-Se phase in abundance, and/or c. the physical barrier faced by Se and/or S molecules to thoroughly interact with the bottom side grains under standard annealing conditions.
6. The bi-layer structure of kesterite devices composed of LG and FG can introduce several problems in the device, including increased series resistance, reduced photon absorption (only LG undergoes photon absorption), increased recombination sites due to excess grain boundaries, and the presence of detrimental carbon-based antisite defects.
7. Ligand exchange strategies are often adopted in literature to replace bulky carbon-rich ligands (OLA, TOPO, OLE) from nanoparticle surfaces with either shorter organic ligands (EDA, EDT, AP) or inorganic ligands (ammonium sulfide, antimony trichloride). Trialkyl oxonium salts can completely strip the carbon-rich ligands from the vicinity of kesterite nanocrystals. Whereas, the use of low-carbon (FA) and green

glycol solvents (EG and DEG) has been opted to simultaneously circumvent CRFG formation and the costly time-consuming ligand exchange/stripping processes.

8. The PLO technique proposed in the perspective to expose the bottom side (carbon-rich) of kesterite film and an extensive compositional study on the exposed surface with XPS depth profiling have revealed that the occupation of CRFG has the potential to cause an increase in series resistance, secondary phases, and bandgap fluctuation which can negatively impact the solar cell performance. This was corroborated by the SCAPS-based simulated response of the CRFG model in the CZTSSe device.

Acknowledgments

The authors appreciate the support from the TUBITAK Grant (No. 120N994) and the British Council Newton Fund Institutional Links Grant (UK-Turkey) in Ultralight Absorber for Remote Energy Source (No. 623804307). The authors also acknowledge the Engineering and Physical Sciences Research Council (EPSRC) Centre for Doctoral Training in Renewable Energy Northeast Universities (ReNU) for funding through grant EP/S023836/1.

Received: ((will be filled in by the editorial staff))
Revised: ((will be filled in by the editorial staff))
Published online: ((will be filled in by the editorial staff))

References

[1] *International Energy Agency (IEA) World Energy Outlook 2023*, **2023**.

[2] A. Varone, Z. Heilmann, G. Porruvecchio, A. Romanino, *Renew. Sustain. Energy Rev.* **2024**, *189*, 113845.

[3] Y. Aziz, A. K. Janjua, M. Hassan, M. Anwar, S. Kanwal, M. Yousif, *Environ. Dev. Sustain.* **2024**, *26*, 5003.

[4] US Department of Energy, *Solar Photovoltaics: Supply Chain Deep Dive Assessment*, **2022**.

[5] M. Woodhouse, R. Jones-Albertus, D. Feldman, R. Fu, K. Horowitz, D. Chung, D. Jordan, S. Kurtz, *Natl. Renew. Energy Lab.* **2016**, 55.

[6] H. Liang, F. You, *Nat. Commun.* **2023**, *14*, 1274.

[7] S. Lee, J. Kim, H. Kwon, D. Son, I. S. Kim, J. Kang, *Nano Energy* **2023**, *110*, 108379.

[8] H. Ke, M. Gao, S. Li, Q. Qi, W. Zhao, X. Li, S. Li, V. Kuvondikov, P. Lv, Q. Wei, L. Ye, *Sol. RRL* **2023**, *7*, 2300109.

[9] B. Wei, X. Mao, W. Liu, C. Ji, G. Yang, Y. Bao, X. Chen, F. Yang, X. Wang, *Plasmonics* **2023**, *18*, 2009.

[10] M. Barbato, E. Artegiani, M. Bertoncello, M. Meneghini, L. Ortolani, E. Zanoni, G. Meneghesso, *J. Phys. D. Appl. Phys.* **2021**, *54*, 333002.

[11] T. D. Lee, A. U. Ebong, *Renew. Sustain. Energy Rev.* **2017**, *70*, 1286.

[12] T. Amrillah, *Sol. Energy* **2023**, *263*, 111982.

[13] N. G. Park, *Mater. Today* **2015**, *18*, 65.

[14] L. Xi, S. Pan, X. Li, Y. Xu, J. Ni, X. Sun, J. Yang, J. Luo, J. Xi, W. Zhu, X. Li, D. Jiang, R. Dronskowski, X. Shi, G. J. Snyder, W. Zhang, *J. Am. Chem. Soc.* **2018**, *140*, 10785.

[15] M. Shaygan, K. Davami, N. Kheirabi, C. K. Baek, G. Cuniberti, M. Meyyappan, J. S. Lee, *Phys. Chem. Chem. Phys.* **2014**, *16*, 22687.

[16] D. Y. Yun, N. S. Arul, D. U. Lee, N. H. Lee, T. W. Kim, *Org. Electron.* **2015**, *24*, 320.

[17] M. Ren, X. Qian, Y. Chen, T. Wang, Y. Zhao, *J. Hazard. Mater.* **2022**, *426*, 127848.

[18] T. T. Werner, G. M. Mudd, S. M. Jowitt, *Ore Geol. Rev.* **2017**, *86*, 939.

[19] L. Grandell, M. Höök, *Sustain.* **2015**, *7*, 11818.

[20] C. C. Boyd, R. Cheacharoen, T. Leijtens, M. D. McGehee, *Chem. Rev.* **2019**, *119*, 3418.

[21] A. Wang, M. He, M. A. Green, K. Sun, X. Hao, *Adv. Energy Mater.* **2023**, *13*, 2203046.

[22] G. Altamura, Development of CZTSSe Thin Films Based Solar Cells, Université Joseph-Fourier-Grenoble I, **2014**.

[23] J. Kim, H. Hiroi, T. K. Todorov, O. Gunawan, M. Kuwahara, T. Gokmen, D. Nair, M. Hopstaken, B. Shin, Y. S. Lee, W. Wang, H. Sugimoto, D. B. Mitzi, *Adv. Mater.* **2014**, *26*, 7427.

[24] J. He, L. Sun, S. Chen, Y. Chen, P. Yang, J. Chu, *J. Alloys Compd.* **2012**, *511*, 129.

[25] K. Ito, T. Nakazawa, *Jpn. J. Appl. Phys.* **1988**, *27*, 2094.

[26] M. P. Suryawanshi, G. L. Agawane, S. M. Bhosale, S. W. Shin, P. S. Patil, J. H. Kim, A. V. Moholkar, *Mater. Technol.* **2013**, *28*, 98.

[27] S. Chen, X. G. Gong, A. Walsh, S. H. Wei, *Appl. Phys. Lett.* **2010**, *96*, 4.

[28] J. Zhong, Z. Xia, M. Luo, J. Zhao, J. Chen, L. Wang, X. Liu, D. Xue, Y. Cheng, H. Song, J. Tang, *Sci. Rep.* **2014**, *4*, 6288.

[29] J. J. Scragg, T. Ericson, T. Kubart, M. Edo, C. Platzer-bj, *ACS Chem. Mater.* **2011**, *23*, 4625.

[30] S. Bourdais, C. Choné, B. Delatouche, A. Jacob, G. Larramona, C. Moisan, A. Lafond, F. Donatini, G. Rey, S. Siebentritt, A. Walsh, G. Dennler, *Adv. Energy Mater.* **2016**, *6*, 1502276.

[31] M. Azzouzi, A. Cabas-vidani, S. G. Haass, J. A. Ro, Y. E. Romanyuk, A. N. Tiwari, J. Nelson, *J. Phys. Chem. Lett.* **2019**, *10*, 2829.

[32] Y. Zhang, Z. Jia, Z. Zhao, *Phys. B Phys. Condens. Matter* **2022**, *626*, 413539.

[33] C. T. Illiyas, K. C. Preetha, *J. Mater. Sci. Mater. Electron.* **2023**, *34*, 1380.

[34] Y. Ji, X. Zhao, Y. Pan, Z. Su, J. Lin, E. M. Akinoglu, Y. Xu, H. Zhang, P. Zhao, Y. Dong, X. Wei, F. Liu, P. Mulvaney, *Adv. Funct. Mater.* **2023**, *33*, 2211421.

[35] P. D. Antunez, D. M. Bishop, Y. S. Lee, T. Gokmen, O. Gunawan, T. S. Gershon, T. K. Todorov, S. Singh, R. Haight, *Adv. Energy Mater.* **2017**, *7*, 1602585.

[36] M. C. Baek, J. S. Jang, M. P. Suryawanshi, V. C. Karade, J. Kim, M. He, S. W. Park, J. H. Kim, S. W. Shin, *J. Alloys Compd.* **2023**, *935*, 167993.

[37] Y. Zhao, Q. Song, Z. Zhou, Y. Chen, Y. Zhang, L. Wu, X. Su, X. Hu, S. Wang, *Sol. Energy* **2023**, *264*, 112005.

[38] H. Honarvar Nazari, T. P. Dhakal, *Sol. Energy* **2023**, *253*, 321.

[39] T. Wu, J. Hu, S. Chen, Z. Zheng, M. Cathelinaud, H. Ma, Z. Su, P. Fan, X. Zhang, G. Liang, *ACS Appl. Mater. Interfaces* **2023**, *15*, 14291.

[40] S. Tao, L. Dong, J. Han, Y. Wang, Q. Gong, J. Wei, M. Zhao, D. Zhuang, *J. Mater. Chem. A* **2023**, *11*, 9085.

[41] X. Li, Z. Hou, S. Gao, Y. Zeng, J. Ao, Z. Zhou, B. Da, W. Liu, Y. Sun, Y. Zhang, *Sol. RRL* **2018**, *2*, 1800198.

[42] Q. Xiao, D. Kou, W. Zhou, Z. Zhou, S. Yuan, Y. Qi, Y. Meng, L. Han, Z. Zheng, S. Wu, *J. Mater. Chem. A* **2023**, *11*, 11161.

[43] Z. Yu, C. Li, S. Chen, Z. Zheng, P. Fan, Y. Li, M. Tan, C. Yan, X. Zhang, Z. Su, G. Liang, *Adv. Energy Mater.* **2023**, *13*, 2300521.

[44] Y. Li, H. Wei, C. Cui, X. Wang, Z. Shao, S. Pang, G. Cui, *J. Mater. Chem. A* **2023**, *11*, 4836.

[45] T. Amrillah, *Sol. Energy* **2023**, *263*, 111982.

[46] M. Kangsabanik, R. N. Gayen, *Sol. RRL* **2023**, *7*, 2300670.

[47] R. Paul, S. Shukla, T. R. Lenka, F. A. Talukdar, V. Goyal, N. E. I. Boukortt, P. S. Menon, *J. Mater. Sci. Mater. Electron.* **2024**, *35*, 226.

[48] U. A. Shah, A. Wang, M. Irfan Ullah, M. Ishaq, I. A. Shah, Y. Zeng, M. S. Abbasi, M. A. Umair, U. Farooq, G. X. Liang, K. Sun, *Small* **2024**, *4*, 2310584.

[49] K. Pal, P. Singh, A. Bhaduri, K. B. Thapa, *Sol. Energy Mater. Sol. Cells* **2019**, *196*, 138.

[50] M. A. Shafi, L. Khan, S. Ullah, M. Y. Shafi, A. Bouich, H. Ullah, B. Mari, *Optik (Stuttg).* **2022**, *253*, 168568.

[51] P. R. Ghediya, J. Silvano, P. Verding, R. Shanivarasanthe Nithyananda Kumar, G. Brammertz, A. Paulus, K. Elen, B. Ruttens, S. Shukla, J. D'Haen, A. Hardy, B. Vermang, W. Deferme, *Appl. Phys. A Mater. Sci. Process.* **2023**, *129*, 404.

[52] Q. Zhao, H. Shen, Y. Xu, K. Gao, D. Chen, Y. Li, *ACS Appl. Energy Mater.* **2022**, *5*, 3668.

[53] F. Mu, Z. Liu, W. Zi, Y. Cao, X. Lu, Y. Li, Z. Zhao, Z. Xiao, N. Cheng, *Sol. Energy* **2021**, *226*, 154.

[54] H. Xu, R. Lang, C. Gao, W. Yu, W. Lu, S. Mohammadi, *Surfaces and Interfaces* **2022**, *33*, 102187.

[55] F. Bouhjar, L. Derbali, Y. H. Khattak, B. Mari, *Opt. Mater. (Amst).* **2024**, *147*, 114582.

[56] S. Campbell, M. Duchamp, B. Ford, M. Jones, L. L. Nguyen, M. C. Naylor, X. Xu, P. Maiello, G. Zoppi, V. Barrioz, N. S. Beattie, Y. Qu, *ACS Appl. Energy Mater.* **2022**, *5*, 5404.

[57] W. M. Hlaing Oo, J. L. Johnson, A. Bhatia, E. A. Lund, M. M. Nowell, M. A. Scarpulla, *J. Electron. Mater.* **2011**, *40*, 2214.

[58] F. Liu, Y. Li, K. Zhang, B. Wang, C. Yan, Y. Lai, Z. Zhang, J. Li, Y. Liu, *Sol. Energy Mater. Sol. Cells* **2010**, *94*, 2431.

[59] U. Syafiq, N. Ataollahi, R. DiMaggio, P. Scardi, *Molecules* **2019**, *24*, 3454.

[60] W. Wang, M. T. Winkler, O. Gunawan, T. Gokmen, T. K. Todorov, Y. Zhu, D. B. Mitzi, *Adv. Energy Mater.* **2014**, *4*, 1301465.

[61] S. Nanthini, K. Sangavi, L. Gowthami, G. S. Dennish Babu, *Optik (Stuttg).* **2020**, *221*, 165342.

[62] "Best research-cell efficiency chart (n.d.)," can be found under https://www.nrel.gov/pv/cell-efficiency.html, **n.d.**

[63] L. Dong, S. Cheng, Y. Lai, H. Zhang, H. Jia, *Thin Solid Films* **2017**, *626*, 168.

[64] X. Yan, X. Hu, S. Komarneni, *J. Korean Phys. Soc.* **2015**, *66*, 1511.

[65] S. M. Bhosale, M. P. Suryawanshi, M. A. Gaikwad, P. N. Bhosale, J. H. Kim, A. V. Moholkar, *Mater. Lett.* **2014**, *129*, 153.

[66] J. Tao, J. Liu, J. He, K. Zhang, J. Jiang, L. Sun, P. Yang, J. Chu, *RSC Adv.* **2014**, *4*, 23977.

[67] Y. Qu, G. Zoppi, N. S. Beattie, *Sol. Energy Mater. Sol. Cells* **2016**, *158*, 130.

[68] S. Campbell, G. Zoppi, L. Bowen, P. Maiello, V. Barrioz, N. S. Beattie, Y. Qu, *ACS Appl. Energy Mater.* **2023**, *6*, 10883.

[69] X. Zhang, E. Fu, Y. Wang, C. Zhang, *Nanomaterials* **2019**, *9*, 336.

[70] S. A. Vanalakar, G. L. Agwane, M. G. Gang, P. S. Patil, J. H. Kim, J. Y. Kim, *Phys. Status Solidi Curr. Top. Solid State Phys.* **2015**, *12*, 500.

[71] G. Chen, C. Yuan, J. Liu, Z. Huang, S. Chen, W. Liu, G. Jiang, C. Zhu, *J. Power Sources* **2015**, *276*, 145.

[72] M. Paris, L. Choubrac, A. Lafond, C. Guillot-Deudon, S. Jobic, *Inorg. Chem.* **2014**, *53*, 8646.

[73] H. Katagiri, K. Jimbo, M. Tahara, H. Araki, K. Oishi, in *Mater. Res. Soc. Symp. Proc. Vol. 1165*, **2009**, pp. 1165-M04-01.

[74] Y. Qu, G. Zoppi, R. W. Miles, N. S. Beattie, *Mater. Res. Express* **2014**, *1*, 045040.

[75] Z. Song, A. B. Phillips, Y. Xie, R. R. Khanal, J. M. Stone, M. J. Heben, in *MRS Online Proc. Libr.*, **2014**, pp. mrsf13-1648-hh03-03.

[76] O. Gunawan, T. K. Todorov, D. B. Mitzi, *Appl. Phys. Lett.* **2010**, *97*, 2008.

[77] S. Bag, O. Gunawan, T. Gokmen, Y. Zhu, D. B. Mitzi, *Chem. Mater.* **2012**, *24*, 4588.

[78] T. K. Todorov, K. B. Reuter, D. B. Mitzi, *Adv. Mater.* **2010**, *22*, E156.

[79] D. A. R. Barkhouse, O. Gunawan, T. Gokmen, D. B. M. Teodor K. Todorov, *Prog. Photovoltaics Res. Appl.* **2012**, *20*, 6.

[80] T. K. Todorov, J. Tang, S. Bag, O. Gunawan, T. Gokmen, Y. Zhu, D. B. Mitzi, *Adv. Energy Mater.* **2013**, *3*, 34.

[81] M. T. Winkler, W. Wang, O. Gunawan, H. J. Hovel, T. K. Todorov, D. B. Mitzi, *Energy Environ. Sci.* **2014**, *7*, 1029.

[82] Yubo Cui, M. Wang, P. Dong, S. Zhang, J. Fu, L. Fan, C. Zhao, S. Wu, Z. Zheng, *Adv. Sci.* **2022**, *9*, 2201241.

[83] Y. Gong, Q. Zhu, B. Li, S. Wang, B. Duan, L. Lou, C. Xiang, E. Jedlicka, R. Giridharagopal, Y. Zhou, Q. Dai, W. Yan, S. Chen, Q. Meng, H. Xin, *Nat. Energy* **2022**, *7*, 966.

[84] X. Pan, X. Li, Y. Yang, C. Xiang, A. Xu, H. Liu, W. Yan, W. Huang, H. Xin, *Adv. Energy Mater.* **2023**, *13*, 2301780.

[85] V. V. Rakitin, P. E. Varushkin, H. Xin, G. F. Novikov, *EPJ Photovoltaics* **2019**, *10*, 6.

[86] Y. Qu, S. W. Chee, M. Duchamp, S. Campbell, G. Zoppi, V. Barrioz, Y. Giret, T. J. Penfold, A. Chaturvedi, U. Mirsaidov, N. S. Beattie, *ACS Appl. Energy Mater.* **2020**, *3*,

122.

[87] Y. Qu, G. Zoppi, N. S. Beattie, *Prog. Photovoltaics Res. Appl.* **2016**, *24*, 836.

[88] Y. Qu, G. Zoppi, L. M. Peter, S. Jourdain, N. S. Beattie, *Jpn. J. Appl. Phys.* **2018**, *57*, 08RC01.

[89] M. C. Naylor, D. Tiwari, A. Sheppard, J. Laverock, S. Campbell, B. Ford, X. Xu, M. D. K. Jones, Y. Qu, P. Maiello, V. Barrioz, N. S. Beattie, N. A. Fox, D. J. Fermin, G. Zoppi, *Faraday Discuss.* **2022**, *239*, 70.

[90] Q. Guo, G. M. Ford, W. C. Yang, C. J. Hages, H. W. Hillhouse, R. Agrawal, *Sol. Energy Mater. Sol. Cells* **2012**, *105*, 132.

[91] Q. Guo, G. M. Ford, W. C. Yang, B. C. Walker, E. A. Stach, H. W. Hillhouse, R. Agrawal, *J. Am. Chem. Soc.* **2010**, *132*, 17384.

[92] Q. Guo, H. W. Hillhouse, R. Agrawal, *J. Am. Chem. Soc.* **2009**, *131*, 11672.

[93] P. Semalti, V. Sharma, S. N. Sharma, *J. Clean. Prod.* **2022**, *365*, 132750.

[94] P. Chawla, S. Jain, P. Vashishtha, M. Ahamed, S. N. Sharma, *Superlattices Microstruct.* **2018**, *113*, 502.

[95] S. Nanthini, K. Sangavi, L. Gowthami, G. S. Dennish Babu, *Optik (Stuttg).* **2020**, *221*, 165342.

[96] T. J. Huang, X. Yin, C. Tang, G. Qi, H. Gong, *J. Mater. Chem. A* **2015**, *3*, 17788.

[97] S. Campbell, Y. Qu, L. Bowen, P. Chapon, V. Barrioz, N. S. Beattie, G. Zoppi, *Sol. Energy* **2018**, *175*, 101.

[98] D. Xia, P. Lei, Y. Zheng, B. Zhou, *J. Mater. Sci. Mater. Electron.* **2015**, *26*, 5426.

[99] N. Ataollahi, F. Bazerla, C. Malerba, A. Chiappini, M. Ferrari, R. Di Maggio, P. Scardi, *Materials (Basel).* **2019**, *12*, 3320.

[100] H. Ahmoum, M. Sukor Su'ait, N. Ataollahi, M. Ubaidah Syafiq Mustaffa, M. Boughrara, P. Chelvanathan, K. Sopian, G. Li, M. Kerouad, P. Scardi, Q. Wang, *Inorg. Chem. Commun.* **2021**, *134*, 109031.

[101] X. Yuan, S. Xue, J. Liao, F. Peng, L. Shao, J. Zhang, *Mater. Res. Express* **2018**, *5*, 016413.

[102] G. Wang, W. Zhao, Y. Cui, Q. Tian, S. Gao, L. Huang, D. Pan, *ACS Appl. Mater. Interfaces* **2013**, *5*, 10042.

[103] S. H. Wu, Y. Y. Wang, K. T. Huang, C. F. Shih, C. W. Chang, C. C. Li, S. W. Chan, *J. Alloys Compd.* **2017**, *703*, 309.

[104] Z. Zou, Y. Gao, F. Long, J. Wang, J. Zhang, *Mater. Lett.* **2015**, *158*, 13.

[105] S. Benny, A. V. Vidyanagar, S. V. Bhat, *Energy and Fuels* **2024**, *38*, 61.

[106] I. Gupta, A. Dey, R. Jain, *Mater. Today Proc.* **2023**, DOI 10.1016/j.matpr.2022.12.106.

[107] J. Fu, J. Yang, W. Dong, S. Ren, H. Zhu, Y. Wang, J. Hao, J. Wu, R. Wang, D. Zhao, Y. Zhang, Z. Zheng, *J. Mater. Chem. A* **2023**, *12*, 545.

[108] L. Wang, Y. Wang, Z. Zhou, W. Zhou, D. Kou, Y. Meng, Y. Qi, S. Yuan, L. Han, S. Wu, *Nanoscale* **2023**, *15*, 8900.

[109] R. Ahmad, M. Distaso, H. Azimi, C. J. Brabec, W. Peukert, *J. Nanoparticle Res.* **2013**, *15*, 1.

[110] X. Xin, D. M. He, W. Han, J. Jung, P. Z. Lin, *Angew. Chemie - Int. Ed.* **2011**, *50*, 11739.

[111] W. H. Zhou, Y. L. Zhou, J. Feng, J. W. Zhang, S. X. Wu, X. C. Guo, X. Cao, *Chem. Phys. Lett.* **2012**, *546*, 115.

[112] X. Xu, Y. Qu, S. Campbell, M. Le Garrec, B. Ford, V. Barrioz, G. Zoppi, N. S. Beattie, *J. Mater. Sci. Mater. Electron.* **2019**, *30*, 7883.

[113] C. J. Hages, M. J. Koeper, C. K. Miskin, K. W. Brew, R. Agrawal, *Chem. Mater.* **2016**, *28*, 7703.

[114] R. A. Zargar, *Metal Oxide Nanocomposite Thin Films for Optoelectronic Device Application*, **2023**.

[115] M. V. Kovalenko, M. Scheele, D. V. Talapinl, *Science (80-.).* **2009**, *324*, 1417.

[116] B. M. Sperry, N. A. Kukhta, Y. Huang, C. K. Luscombe, *Chem. Mater.* **2023**, *35*, 570.

[117] K. Tanaka, M. Kato, H. Uchiki, *J. Alloys Compd.* **2014**, *616*, 492.

[118] J. van Embden, A. S. R. Chesman, E. Della Gaspera, N. W. Duffy, S. E. Watkins, J. J. Jasieniak, *J. Am. Chem. Soc.* **2014**, *136*, 5237.

[119] S. Campbell, Y. Qu, J. Gibbon, H. J. Edwards, V. R. Dhanak, D. Tiwari, V. Barrioz, N. S. Beattie, G. Zoppi, *J. Appl. Phys.* **2020**, *127*, 205305.

[120] R. Mainz, B. C. Walker, S. S. Schmidt, O. Zander, A. Weber, H. Rodriguez-Alvarez, J. Just, M. Klaus, R. Agrawal, T. Unold, *Phys. Chem. Chem. Phys.* **2013**, *15*, 18281.

[121] G. Bree, C. Coughlan, H. Geaney, K. M. Ryan, *ACS Appl. Mater. Interfaces* **2018**, *10*, 7117.

[122] W. Wu, Y. Cao, J. V. Caspar, Q. Guo, L. K. Johnson, I. Malajovich, H. D. Rosenfeld, K. R. Choudhury, *J. Mater. Chem. C* **2014**, *2*, 3777.

[123] D. Hauschild, S. J. Wachs, W. Kogler, L. Seitz, J. Carter, T. Schnabel, B. Krause, M. Blum, W. Yang, E. Ahlswede, C. Heske, L. Weinhardt, *IEEE J. Photovoltaics* **2021**, *11*, 658.

[124] B. A. Williams, M. A. Smeaton, N. D. Trejo, L. F. Francis, E. S. Aydil, *Chem. Mater.*

2017, *29*, 1676.

[125] V. T. Tiong, Y. Zhang, J. Bell, H. Wang, *RSC Adv.* **2015**, *5*, 20178.

[126] M. Burgelman, K. Decock, A. Niemegeers, J. Verschraegen, S. Degrave, *SCAPS Manual*, **2020**.

[127] J. Zhu, M. C. Hersam, *Adv. Mater.* **2017**, *29*, 1603895.

[128] H. Wu, D. Kong, Z. Ruan, P. C. Hsu, S. Wang, Z. Yu, T. J. Carney, L. Hu, S. Fan, Y. Cui, *Nat. Nanotechnol.* **2013**, *8*, 421.

[129] S. I. Kakherskyi, O. A. Dobrozhan, R. M. Pshenychnyi, S. I. Vorobiov, Y. O. Havryliuk, V. Komanicky, S. V. Plotnikov, A. S. Opanasyuk, *Mater. Sci.* **2022**, *57*, 572.

[130] S. Peng, S. Zhang, S. G. Mhaisalkar, S. Ramakrishna, *Phys. Chem. Chem. Phys.* **2012**, *14*, 8523.

[131] J. T. Siy, E. M. Brauser, M. H. Bartl, *Chem. Commun.* **2011**, *47*, 364.

[132] H. Zhou, W. C. Hsu, H. S. Duan, B. Bob, W. Yang, T. Bin Song, C. J. Hsu, Y. Yang, *Energy Environ. Sci.* **2013**, *6*, 2822.

[133] F. M. de Souza, R. K. Gupta, *Nano-Inks: Fundamentals, Synthesis, and Energy Applications*, Elsevier, **2022**.

[134] W. Ahmad, J. He, Z. Liu, K. Xu, Z. Chen, X. Yang, D. Li, Y. Xia, J. Zhang, C. Chen, *Adv. Mater.* **2019**, *31*, 1900593.

[135] A. Cho, S. Ahn, J. H. Yun, J. Gwak, H. Song, K. Yoon, *J. Mater. Chem.* **2012**, *22*, 17893.

[136] S. Jain, P. Chawla, S. N. Sharma, D. Singh, N. Vijayan, *Superlattices Microstruct.* **2018**, *119*, 59.

[137] M. G. Panthani, V. Akhavan, B. Goodfellow, J. P. Schmidtke, L. Dunn, A. Dodabalapur, P. F. Barbara, B. A. Korgel, *J. Am. Chem. Soc.* **2008**, *130*, 16770.

[138] R. Khosroshahi, N. A. Tehrani, M. Forouzandeh, F. Behrouznejad, N. Taghavinia, M. Bagherzadeh, *J. Ind. Eng. Chem.* **2022**, *106*, 253.

[139] R. W. Crisp, M. G. Panthani, W. L. Rance, J. N. Duenow, P. A. Parilla, R. Callahan, M. S. Dabney, J. J. Berry, D. V. Talapin, J. M. Luther, *ACS Nano* **2014**, *8*, 9063.

[140] V. A. Akhavan, B. W. Goodfellow, M. G. Panthani, C. Steinhagen, T. B. Harvey, C. J. Stolle, B. A. Korgel, *J. Solid State Chem.* **2012**, *189*, 2.

[141] C. Y. Peng, T. P. Dhakal, S. Garner, P. Cimo, S. Lu, C. R. Westgate, *Thin Solid Films* **2014**, *562*, 574.

[142] P. R. Ghediya, T. K. Chaudhuri, D. Vankhade, *J. Alloys Compd.* **2016**, *685*, 498.

[143] Y. Cao, M. S. Denny, J. V. Caspar, W. E. Farneth, Q. Guo, A. S. Ionkin, L. K. Johnson, M. Lu, I. Malajovich, D. Radu, H. D. Rosenfeld, K. R. Choudhury, W. Wu, *J. Am. Chem. Soc.* **2012**, *134*, 15644.

[144] S. Hadke, M. Huang, C. Chen, Y. F. Tay, S. Chen, J. Tang, L. Wong, *Chem. Rev.* **2022**, *122*, 10170.

[145] P. Dai, Y. Zhang, Y. Xue, X. Jiang, X. Wang, J. Zhan, Y. Bando, *Mater. Lett.* **2015**, *158*, 198.

[146] C. K. Miskin, W. C. Yang, C. J. Hages, N. J. Carter, C. S. Joglekar, E. A. Stach, R. Agrawal, *Prog. Photovoltaics Res. Appl.* **2015**, *23*, 654.

[147] J. Fu, J. Yang, W. Dong, S. Ren, H. Zhu, Y. Wang, J. Hao, J. Wu, R. Wang, D. Zhao, Y. Zhang, Z. Zheng, *J. Mater. Chem. A* **2024**, *12*, 545.

[148] T. K. Todorov, J. Tang, S. Bag, O. Gunawan, T. Gokmen, Y. Zhu, D. B. Mitzi, *Adv. Energy Mater.* **2013**, *3*, 34.

[149] R. Zhang, S. M. Szczepaniak, N. J. Carter, C. A. Handwerker, R. Agrawal, *Chem. Mater.* **2015**, *27*, 2114.

[150] J. C. Lowe, L. D. Wright, D. B. Eremin, J. V. Burykina, J. Martens, F. Plasser, V. P. Ananikov, J. W. Bowers, A. V. Malkov, *J. Mater. Chem. C* **2020**, *8*, 10309.

[151] M. Node, K. Kumar, K. Nishide, S. I. Ohsugi, T. Miyamoto, *Tetrahedron Lett.* **2001**, *42*, 9207.

[152] Y. Gong, Y. Zhang, Q. Zhu, Y. Zhou, R. Qiu, C. Niu, W. Yan, W. Huang, H. Xin, *Energy Environ. Sci.* **2021**, *14*, 2369.

[153] I. G. Orletskyi, M. M. Solovan, V. V. Brus, F. Pinna, G. Cicero, P. D. Maryanchuk, E. V. Maistruk, M. I. Ilashchuk, T. I. Boichuk, E. Tresso, *J. Phys. Chem. Solids* **2017**, *100*, 154.

[154] H. Luan, B. Yao, Y. Li, R. Liu, Z. Ding, Y. Sui, Z. Zhang, H. Zhao, L. Zhang, *Sol. Energy Mater. Sol. Cells* **2019**, *195*, 55.

[155] C. Niu, Y. Gong, R. Qiu, Q. Zhu, Y. Zhou, S. Hao, W. Yan, W. Huang, H. Xin, *J. Mater. Chem. A* **2021**, *9*, 12981.

[156] F. Liu, S. Shen, F. Zhou, N. Song, X. Wen, J. A. Stride, K. Sun, C. Yan, X. Hao, *J. Mater. Chem. C* **2015**, *3*, 10783.

[157] C. Coughlan, K. M. Ryan, *CrystEngComm* **2015**, *17*, 6914.

[158] Y. Zhao, C. Xu, N. Yu, Z. Zhou, Y. Chen, X. Hu, Y. Zhang, S. Wang, *Sol. Energy* **2023**, *258*, 294.

[159] S. Ge, H. Gao, R. Hong, J. Li, Y. Mai, X. Lin, G. Yang, *ChemSusChem* **2019**, *12*,

1478.

[160] Z. Su, G. Liang, P. Fan, J. Luo, Z. Zheng, Z. Xie, W. Wang, S. Chen, J. Hu, Y. Wei, C. Yan, J. Huang, X. Hao, F. Liu, *Adv. Mater.* **2020**, *32*, 2000121.

[161] A. D. Collord, H. W. Hillhouse, *Chem. Mater.* **2016**, *28*, 2067.

[162] S. H. Hadke, S. Levcenko, S. Lie, C. J. Hages, J. A. Márquez, T. Unold, L. H. Wong, *Adv. Energy Mater.* **2018**, *8*, 1802540.

[163] H. Dong, T. Schnabel, E. Ahlswede, C. Feldmann, *Solid State Sci.* **2014**, *29*, 52.

[164] B. D. Chernomordik, A. E. Béland, D. D. Deng, L. F. Francis, E. S. Aydil, *Chem. Mater.* **2014**, *26*, 3191.

[165] U. V. Ghorpade, M. P. Suryawanshi, S. W. Shin, C. W. Hong, I. Kim, J. H. Moon, J. H. Yun, J. H. Kim, S. S. Kolekar, *Phys. Chem. Chem. Phys.* **2015**, *17*, 19777.

[166] Y. Kim, K. Woo, I. Kim, Y. S. Cho, S. Jeong, J. Moon, *Nanoscale* **2013**, *5*, 10183.

[167] M. Zhou, Y. Gong, J. Xu, G. Fang, Q. Xu, J. Dong, *J. Alloys Compd.* **2013**, *574*, 272.

[168] R. G. Ellis, J. W. Turnley, D. J. Rokke, J. P. Fields, E. H. Alruqobah, S. D. Deshmukh, K. Kisslinger, R. Agrawal, *Chem. Mater.* **2020**, *32*, 5091.

[169] S. C. Riha, B. A. Parkinson, A. L. Prieto, *J. Am. Chem. Soc.* **2009**, *131*, 12054.

[170] W. C. Chen, V. Tunuguntla, M. H. Chiu, L. J. Li, I. Shown, C. H. Lee, J. S. Hwang, L. C. Chen, K. H. Chen, *Sol. Energy Mater. Sol. Cells* **2017**, *161*, 416.

[171] A. Kulendran, J. Bell, H. Wang, in *Fourth Int. Conf. Smart Mater. Nanotechnol. Eng.*, **2013**, p. 87931A.

[172] S. Jain, D. Singh, N. Vijayan, S. N. Sharma, *Appl. Nanosci.* **2018**, *8*, 435.

[173] N. Mirbagheri, S. Engberg, A. Crovetto, S. B. Simonsen, O. Hansen, Y. M. Lam, J. Schou, *Nanotechnology* **2016**, *27*, 185603.

[174] S. Campbell, Y. Qu, L. Bowen, P. Chapon, V. Barrioz, N. S. Beattie, G. Zoppi, *Sol. Energy* **2018**, *175*, 101.

[175] T. J. Huang, X. Yin, C. Tang, G. Qi, H. Gong, *ChemSusChem* **2016**, *9*, 1032.

[176] E. M. Mkawi, Y. Al-Hadeethi, E. Shalaan, E. Bekyarova, *Appl. Phys. A Mater. Sci. Process.* **2020**, *126*, 50.

[177] B. D. Chernomordik, A. E. Béland, N. D. Trejo, A. A. Gunawan, D. D. Deng, K. A. Mkhoyan, E. S. Aydil, *J. Mater. Chem. A* **2014**, *2*, 10389.

[178] S. Ananthakumar, J. R. Kumar, S. M. Babu, *Optik (Stuttg).* **2017**, *130*, 99.

[179] R. Ahmad, K. S. Nicholson, Q. Nawaz, W. Peukert, M. Distaso, *J. Nanoparticle Res.* **2017**, *19*, 1.

[180] H. Jiang, P. Dai, Z. Feng, W. Fan, J. Zhan, *J. Mater. Chem.* **2012**, *22*, 7502.

[181] C. Sripan, D. Alagarasan, S. Varadharajaperumal, R. Ganesan, R. Naik, *Curr. Appl. Phys.* **2020**, *20*, 925.

[182] J. Joo, H. Bin Na, T. Yu, J. H. Yu, Y. W. Kim, F. Wu, J. Z. Zhang, T. Hyeon, *J. Am. Chem. Soc.* **2003**, *125*, 11100.

[183] C. Steinhagen, G. M. Panthani, V. Akhavan, B. Goodfellow, B. Koo, B. A. Korgel, *J. Am. Chem. Soc.* **2009**, *131*, 12554.

[184] A. Méndez-López, A. Morales-Acevedo, Y. J. Acosta-Silva, M. Ortega-López, *J. Nanomater.* **2016**, *1*, 7486094.

[185] G. M. Ford, Q. Guo, R. Agrawal, H. W. Hillhouse, *Chem. Mater.* **2011**, *23*, 2626.

[186] S. C. Riha, B. a Parkinson, A. L. Prieto, *J. Am. Chem. Soc.* **2011**, *133*, 15272.

[187] G. M. Ilari, C. M. Fella, C. Ziegler, A. R. Uhl, Y. E. Romanyuk, A. N. Tiwari, *Sol. Energy Mater. Sol. Cells* **2012**, *104*, 125.

[188] Y. S. Lee, T. Gershon, O. Gunawan, T. K. Todorov, T. Gokmen, Y. Virgus, S. Guha, *Adv. Energy Mater.* **2015**, *5*, 1401372.

[189] T. Taskesen, J. Neerken, J. Schoneberg, D. Pareek, V. Steininger, J. Parisi, L. Gütay, *Adv. Energy Mater.* **2018**, *8*, 4.

[190] C. M. Fella, A. R. Uhl, Y. E. Romanyuk, A. N. Tiwari, *Phys. Status Solidi Appl. Mater. Sci.* **2012**, *209*, 1043.

[191] S. Campbell, M. Duchamp, B. Ford, M. Jones, L. L. Nguyen, M. C. Naylor, X. Xu, P. Maiello, G. Zoppi, V. Barrioz, N. S. Beattie, *ACS Appl. Energy Mater.* **2022**, *5*, 5404.

[192] M. H. Sayed, M. Brandl, C. Chory, I. Hammer-riedel, J. Parisi, L. Gütay, R. Hock, *J. Alloys Compd.* **2016**, *686*, 24.

[193] K. C. Wang, H. R. Hsu, H. S. Chen, *Sol. Energy Mater. Sol. Cells* **2017**, *163*, 31.

[194] B. D. Chernomordik, P. M. Ketkar, A. K. Hunter, A. E. Béland, D. D. Deng, E. S. Aydil, *Chem. Mater.* **2016**, *28*, 1266.

[195] D. J. G. Ives, R. W. Pittman, W. Wardlaw, *J. Chem. Soc.* **1947**, 1080.

[196] Q. Yan, S. Cheng, H. Li, X. Yu, J. Fu, Q. Tian, H. Jia, S. Wu, *Sol. Energy* **2019**, *177*, 508.

[197] S. Chen, H. Tao, Y. Shen, L. Zhu, X. Zeng, J. Tao, T. Wang, *RSC Adv.* **2015**, *5*, 6682.

[198] F. Takagi, Y. Kageshima, K. Teshima, K. Domen, H. Nishikiori, *Sustain. Energy Fuels* **2021**, *5*, 412.

[199] X. Lin, J. Kavalakkatt, A. Ennaoui, M. C. Lux-Steiner, *Sol. Energy Mater. Sol. Cells* **2015**, *132*, 221.

[200] H. Ahmoum, M. Boughrara, M. S. Su'ait, G. Li, S. Chopra, Q. Wang, M. Kerouad,

Mater. Chem. Phys. **2020**, *251*, 123065.

[201] D. Mutter, S. T. Dunham, *IEEE J. Photovoltaics* **2016**, *6*, 562.

[202] K. E. Roelofs, Q. Guo, S. Subramoney, J. V. Caspar, *J. Mater. Chem. A* **2014**, *2*, 13464.

[203] M. Park, S. Ahn, J. H. Yun, J. Gwak, A. Cho, S. Ahn, K. Shin, D. Nam, H. Cheong, K. Yoon, *J. Alloys Compd.* **2012**, *513*, 68.

[204] S. Suehiro, K. Horita, K. Kumamoto, M. Yuasa, T. Tanaka, K. Fujita, K. Shimanoe, T. Kida, *J. Phys. Chem. C* **2014**, *118*, 804.

[205] L. S. Khanzada, I. Levchuk, Y. Hou, H. Azimi, A. Osvet, R. Ahmad, M. Brandl, P. Herre, M. Distaso, R. Hock, W. Peukert, M. Batentschuk, C. J. Brabec, *Adv. Funct. Mater.* **2016**, *26*, 8300.

[206] A. Carrete, A. Shavel, X. Fontané, J. Montserrat, J. Fan, M. Ibáñez, E. Saucedo, A. Pérez-Rodríguez, A. Cabot, *J. Am. Chem. Soc.* **2013**, *135*, 15982.

[207] I. Kim, K. Kim, Y. Oh, K. Woo, G. Cao, S. Jeong, J. Moon, *Chem. Mater.* **2014**, *26*, 3957.

[208] Z. Gong, Q. Han, J. Li, L. Hou, A. Bukhtiar, S. Yang, B. Zou, *J. Alloys Compd.* **2016**, *663*, 617.

[209] S. N. Park, S. J. Sung, D. H. Son, D. H. Kim, M. Gansukh, H. Cheong, J. K. Kang, *RSC Adv.* **2014**, *4*, 9118.

[210] W. Kogler, T. Schnabel, E. Ahlswede, M. Powalla, *Sol. Energy Mater. Sol. Cells* **2019**, *200*, 109959.

[211] S. Nath, S. Jana, M. Pradhan, T. Pal, *J. Colloid Interface Sci.* **2010**, *341*, 333.

[212] A. Heuer-Jungemann, N. Feliu, I. Bakaimi, M. Hamaly, A. Alkilany, I. Chakraborty, A. Masood, M. F. Casula, A. Kostopoulou, E. Oh, K. Susumu, M. H. Stewart, I. L. Medintz, E. Stratakis, W. J. Parak, A. G. Kanaras, *Chem. Rev.* **2019**, *119*, 4819.

[213] Y. Liu, M. Gibbs, J. Puthussery, S. Gaik, R. Ihly, H. W. Hillhouse, M. Law, *Nano Lett.* **2010**, *10*, 1960.

[214] W. Huang, Q. Li, Y. Chen, Y. Xia, H. Huang, C. Dun, Y. Li, D. L. Carroll, *Sol. Energy Mater. Sol. Cells* **2014**, *127*, 188.

[215] S. K. Saha, A. Guchhait, A. J. Pal, *Phys. Chem. Chem. Phys.* **2012**, *14*, 8090.

[216] W. K. Metzger, M. Gloeckler, *J. Appl. Phys.* **2005**, *98*, 063701.

[217] X. Liu, F. Zhou, N. Song, J. Huang, C. Yan, F. Liu, K. Sun, J. A. Stride, X. Hao, M. A. Green, *J. Mater. Chem. A* **2015**, *3*, 23185.

[218] S.-H. Wu, C.-W. Chang, H.-J. Chen, C.-F. Shih, Y.-Y. Wang, C.-C. Li, S.-W. Chan,

Prog. Photovoltaics Res. Appl. **2016**, *25*, 58.

[219] L. Korala, M. B. Braun, J. M. Kephart, Z. Tregillus, A. L. Prieto, *Chem. Mater.* **2017**, *29*, 6621.

[220] E. L. Rosen, R. Buonsanti, A. Llordes, A. M. Sawvel, D. J. Milliron, B. A. Helms, *Angew. Chemie - Int. Ed.* **2012**, *51*, 684.

[221] C. Jiang, J. Lee, D. V Talapin, *J. Am. Chem. Soc* **2012**, *134*, 5010.

[222] C. B. Murray, C. R. Kagan, M. G. Bawendi, *Annu. Rev. Mater. Sci.* **2006**, *30*, 545.

[223] C. Imla Mary, M. Senthilkumar, G. Manobalaji, M. Sai Prasanna, S. Moorthy Babu, *J. Mater. Sci. Mater. Electron.* **2022**, *33*, 894.

[224] N. C. Anderson, M. P. Hendricks, J. J. Choi, J. S. Owen, *J. Am. Chem. Soc.* **2013**, *135*, 18536.

[225] D. B. Mitzi, L. L. Kosbar, C. E. Murray, M. Copel, A. Afzali, *Nature* **2004**, *428*, 299.

[226] A. Nag, M. V. Kovalenko, J. S. Lee, W. Liu, B. Spokoyny, D. V. Talapin, *J. Am. Chem. Soc.* **2011**, *133*, 10612.

[227] Z. X. Zhang, Z. J. Zhou, B. Bai, M. H. Liu, W. H. Zhou, D. X. Kou, S. X. Wu, *J. Nanoparticle Res.* **2015**, *17*, 1.

[228] C. I. Mary, M. Senthilkumar, G. Manobalaji, S. M. Babu, *J. Mater. Sci. Mater. Electron.* **2020**, *31*, 18164.

[229] M. Sai Prasanna, C. Imla Mary, M. Senthilkumar, G. Manobalaji, S. Moorthy Babu, *Phys. Status Solidi Basic Res.* **2022**, *259*, 2100309.

[230] M. B. Braun, L. Korala, J. M. Kephart, A. L. Prieto, *ACS Appl. Energy Mater.* **2018**, *1*, 1053.

[231] S. Suehiro, K. Horita, K. Kumamoto, M. Yuasa, T. Tanaka, K. Fujita, K. Shimanoe, T. Kida, *J. Phys. Chem. C* **2014**, *118*, 804.

[232] P. Kush, S. K. Ujjain, N. C. Mehra, P. Jha, R. K. Sharma, S. Deka, *ChemPhysChem* **2013**, *14*, 2793.

[233] W. Wang, H. Shen, L. H. Wong, Z. Su, H. Yao, Y. Li, *RSC Adv.* **2016**, *6*, 54049.

[234] A. Javed, M. Jones, S. Campbell, S. Yerci, V. Barrioz, Y. Qu, *Adv. Mater. Interfaces* **2024**, *11*, 2300715.

Hot injection with organic solvents is a prevalent technique to fabricate kesterite nanofilms. However, this process leads to the formation of carbon-rich fine grains (CRFG) in the finished layer post-annealing treatment. The nanocrystals in CRFG are encompassed by decomposed carbon matrices which can account for enhanced series resistance in addition to introducing abundant grain boundaries and secondary phases. Unwanted carbon-rich ligands are removed using ligand exchange/stripping agents from the surface of kesterite nanocrystals.

Ahmed Javed, Doguscan Donmez, Michael D.K Jones, Yongtao Qu*, Gorkem Gunbas, Selcuk Yerci*

Kesterite Films Processed with Organic Solvents: Unveiling the Impact of Carbon-Rich Fine Grain Layer Formation on Solar Cell Performance

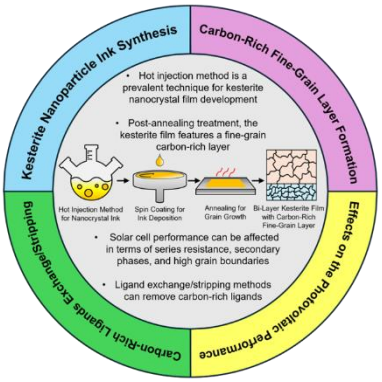

Dr. Selcuk Yerci is head of the test and characterization team at ODTU-GUNAM in addition to working as an Associate Professor at the Electrical/Electronics Engineering Department, Middle East Technical University, Ankara, Turkiye. In 2011, Dr. Yerci received a PhD. in Electrical Engineering from Boston University, USA, and later a post-doctorate from Massachusetts Institute of Technology, USA. He has been involved in quality research in the fields of photonics, optoelectronic devices, and renewable energy technology. Currently, Dr. Yerci is doing research and development work on many projects including thin film characterizations, perovskite solar cells, and tandem photovoltaic devices.

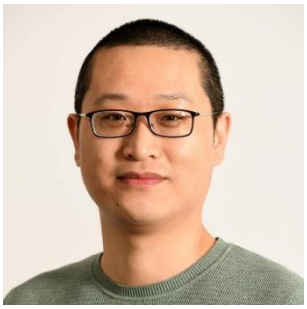

Dr. Yongtao Qu is an Associate Professor at the Physics Department, at Northumbria University, UK. His research interests focus on developing light-absorbing layers and structures for the generation of clean and renewable electricity. Dr. Qu received his PhD. in Physics from Northumbria University, UK in 2016. Dr Qu is directly contributing as the Centre Manager to the running of the EPSRC Centre for Doctoral Training in Renewable Energy Northeast Universities (ReNU). Dr. Qu is an expert in solution-processed fabrication techniques for developing nanofilms and has been an active researcher in kesterite technology.

Ahmed Javed completed his BS. and MS. degrees in Electrical Engineering in 2017 and 2019, respectively. Currently, he is pursuing his PhD. in the Micro and Nanotechnology Program at Middle East Technical University, Ankara, Turkiye. Mr. Javed's research interests are focused on nano-fabrication and nano-characterization techniques for thin films.